

ARTICLE OPEN



Homozygous CHD8 mutation intensifies ASD phenotypes and attenuates sex differences

Jinkyong Kim^{1,8}, Seungjoon Lee^{2,8}, Eunkyu Hwang^{3,8}, Hwajin Jung², Chanhee Lee^{4,5}, Sang-Han Choi^{4,5}, Sooyeon Lee¹, Seongbin Kim¹, Heera Moon¹, Jisoo Kim¹, Gina Lee¹, Yong Gyu Kim², Soogeun Shin³, Hyojin Kang⁶, Se Jin Kim⁷, Heon Yung Gee⁷, Seong-Gi Kim^{4,5}, Eunee Lee^{2,3} and Eunjoon Kim^{1,2}

© The Author(s) 2026

CHD8 is a chromatin remodeler implicated in autism spectrum disorders (ASD) and multiple neurodevelopmental disorders, yet heterozygous *Chd8*-mutant mouse lines often exhibit only mild ASD-related phenotypes, leaving its role unclear. Because a complete knockout of *Chd8* causes embryonic lethality, we generated viable homozygous *Chd8*-mutant mice carrying the human CHD8-Asn2373LysfsX2 mutation using a hybrid (C57BL6/J × 129/Sv) genetic background. Compared to heterozygous *Chd8*^{+/*N2373K*} mice, the homozygous *Chd8*^{*N2373K/N2373K*} mice showed more robust phenotypes, including increased ASD-related behaviors and brain volume, decreased cerebral blood volume/flow, brain rhythms, and synaptic transmission, and ASD-related transcriptomic changes. Notably, while *Chd8*^{+/*N2373K*} mice on a pure background predominantly displayed behavioral deficits in males, the homozygous mutants in the hybrid background exhibited more pronounced female phenotypes, suggesting the interaction of genetic background and mutation strength. A direct comparison of *Chd8*^{+/*N2373K*} and *Chd8*^{*N2373K/N2373K*} mice on the same hybrid background across brain volume, cerebral blood flow, neuronal firing, synaptic transmission, and transcriptome revealed a gene dosage-dependent attenuation of sexual dimorphic phenotypes that varied by developmental stage and brain region. Transcriptomic analyses further implicated pathways related to synaptic function, RNA splicing, and mitochondrial activity in mediating differences in male–female protection and susceptibility. Thus, a homozygous *Chd8* mutation not only intensifies ASD-related traits but can also diminish typical sex-specific severity patterns, uncovering a novel link between mutation strength and sexual dimorphism in ASD.

Molecular Psychiatry; <https://doi.org/10.1038/s41380-026-03646-9>

INTRODUCTION

CHD8, encoding a chromatin remodeler, is implicated in approximately 0.2–0.4% of ASD cases [1–7] as well as in other neurodevelopmental disorders such as intellectual disability, developmental delay, ADHD, neurological problems, sleep disturbances, and schizophrenia [8, 9]. CHD8 influences many other ASD-risk genes and is critical for neural development and function [10], as demonstrated by studies, including those using *Chd8*-mutant mice [10–48]. While murine models recapitulate aspects of CHD8-related pathology (e.g., macrocephaly), behavioral phenotypes often fail to robustly mirror core ASD-like phenotypes (e.g., repetitive behavior), complicating mechanistic investigations [11–13, 17, 19, 21, 32, 45]. This is partly because homozygous *Chd8* mutation usually leads to embryonic lethality in mice, although hypomorphic *Chd8* mutants have been reported to display gene deletion dosage-dependent variations in transcriptomic and brain size phenotypes [31].

We previously reported heterozygous *Chd8*-mutant mice carrying the patient-derived knock-in mutation Asn2373LysfsX2

(*Chd8*^{+/*N2373K*} mice) [19, 49]. These mice exhibit male-preponderant molecular, synaptic, neuronal, and behavioral phenotypes reminiscent of ASD [19], similar to the results from human genetics [4, 50] and other *Chd8*-mutant mice [35], although homozygous mutant (*Chd8*^{*N2373K/N2373K*}) mice were embryonically lethal, preventing us from observing stronger behavioral phenotypes and exploring underlying mechanisms [19]. Notably, female *Chd8*^{+/*N2373K*} mice appeared to possess protective neurobiological features such as reduced baseline neuronal excitability and elevated inhibitory synaptic transmission and inhibitory neuronal firing [19] that may mitigate ASD-like impairments, rendering the phenotypes in male *Chd8*^{+/*N2373K*} mice more pronounced. If these female protective effects are correct, then a stronger *Chd8* mutation might overpower them, resulting in deficits in both male and female mutants and providing direct evidence for gene dosage-dependent suppression of sexually dimorphic phenotypes in ASD. Producing viable *Chd8*^{*N2373K/N2373K*} mice would allow us to address these two key research aims.

¹Department of Biological Sciences, Korea Advanced Institute of Science and Technology (KAIST), Daejeon, Korea. ²Center for Synaptic Brain Dysfunctions, Institute for Basic Science (IBS), Daejeon, Korea. ³Department of Anatomy, Graduate School of Medical Science, Yonsei University College of Medicine, Brain Korea 21 Project, Seoul, Korea. ⁴Center for Neuroscience Imaging Research, Institute for Basic Science (IBS), Suwon, Korea. ⁵Department of Biomedical Engineering, Sungkyunkwan University, Suwon, Korea. ⁶Division of National Supercomputing, Korea Institute of Science and Technology Information (KISTI), Daejeon, Korea. ⁷Department of Pharmacology, Graduate School of Medical Science, Yonsei University College of Medicine, Brain Korea 21 Project, Seoul, Korea. ⁸These authors contributed equally: Jinkyong Kim, Seungjoon Lee, Eunkyu Hwang.

✉email: EUNEE@yuhs.ac; kime@kaist.ac.kr

Received: 5 March 2025 Revised: 7 April 2026 Accepted: 30 April 2026

Published online: 09 May 2026

To overcome embryonic lethality, we switched the genetic background of *Chd8*^{N2373K/N2373K} mice from pure C57BL6/J to a hybrid (C57BL6/J × 129/Sv) background, which rescued the viability of homozygous mutants. On this hybrid background, *Chd8*^{N2373K/N2373K} mice displayed more severe behavioral deficits compared to *Chd8*^{+N2373K} mice, with these deficits being notably more pronounced in females, a stark contrast to the patterns observed on the pure background. Comprehensive assessments, including brain volume (MRI), cerebral blood volume/flow (fMRI), neuronal firing, synaptic function, and transcriptomic profiling—revealed a gene dosage-dependent intensification of phenotypes alongside suppressed and, in specific molecular readouts, partially reconfigured sexual dimorphism.

RESULTS

Generation of viable homozygous *Chd8*^{N2373K/N2373K} mice

Our previous study using *Chd8*-mutant mice with a human CHD8 frameshift mutation (N2373KfsX) [49] showed male-preponderant phenotypes in heterozygous (*Chd8*^{+N2373K}) mice [19]. Investigating homozygous (*Chd8*^{N2373K/N2373K}) mice could reveal stronger core ASD-related traits, such as increased self-grooming, and help assess how mutation strength affects sexual dimorphism. However, embryonic lethality has hindered this line of research. To address this limitation, we switched the genetic background from pure C57BL6/J to a hybrid C57BL6/J × 129/Sv (Fig. 1a), a strategy known to mitigate lethality through enhanced genetic diversity and buffering of deleterious mutations [51].

This change markedly suppressed the embryonic lethality and normalized the Mendelian ratios of wild-type (WT), *Chd8*^{+N2373K}, and *Chd8*^{N2373K/N2373K} mice (Fig. 1b). *Chd8* mRNAs in hybrid-background *Chd8*^{N2373K/N2373K} mice were reduced to ~40–50% of WT levels (Fig. 1c), suggestive of nonsense-mediated decay. CHD8 proteins in *Chd8*^{N2373K/N2373K} mice were decreased to ~20% of WT levels, as shown by immunoblot results using N- and C-terminal-targeting antibodies and whole-brain and brain region-specific lysates (Fig. 1d–f; Supplementary Fig. 1), suggesting that the truncated CHD8 proteins lacking the last ~200 aa residues are unstable, and their levels are reduced to ~20% of WT levels.

Sexually dimorphic behavioral deficits in *Chd8*^{N2373K/N2373K} mice

We next subjected *Chd8*^{+N2373K} and *Chd8*^{N2373K/N2373K} males and females to a series of ASD-related behavioral tests assessing locomotor activity, anxiety-like behavior, repetitive behavior, and social interaction (Fig. 2a).

Chd8^{+N2373K} mice on the hybrid background did not exhibit significant behavioral changes (Fig. 2b–k; summarized in Fig. 2; Supplementary Table 1). This contrasts with the male-preponderant deficits observed in *Chd8*^{+N2373K} mice on a pure background, suggesting that the hybrid background may buffer against the development of ASD-like behaviors.

In homozygous *Chd8*^{N2373K/N2373K} mice, females exhibited strong behavioral deficits, including open-field hypoactivity, anxiety-like behavior (open-field and light–dark but not elevated plus-maze tests), increased self-grooming in the Laboras cages (familiar environment) but not in the home cages (novel environment), and abnormally enhanced social interaction in the direct-interaction but not the three-chamber test, as compared with WT females (Fig. 2a–l). *Chd8*^{N2373K/N2373K} males showed qualitatively similar changes, but, apart from Laboras self-grooming, most measures did not reach statistical significance. Notably, Laboras self-grooming was significantly increased in mutant males relative to WT males, paralleling the robust increase observed in mutant females. Reintroducing outliers initially excluded by Grubbs' test preserved the overall male–female difference patterns, though some female traits, namely open-field hypoactivity, open-field

anxiety, and Laboras self-grooming, lost statistical significance (Supplementary Fig. 2; Supplementary Table 1).

These results indicate that a homozygous *Chd8* mutation elicits stronger behavioral changes than a heterozygous mutation, establishing a robust causal link between CHD8 mutation and mouse behavioral deficits, a relationship that was less evident for core ASD-like behaviors (i.e., self-grooming) in earlier studies. Consistent with our effect-size analysis (Cohen's *d*; Supplementary Table 1), *Chd8*^{N2373K/N2373K} females display more large effects ($|d| \geq 0.8$) than males across the behavioral battery: in males, a large effect is mainly evident for Laboras grooming in the WT versus HM comparison, whereas in females large effects occur for Laboras grooming, open-field locomotor activity, open-field center time, and direct interaction (WT vs HM), as well as for direct interaction (WT vs HT). Together with the group variances (Supplementary Table 1), these findings suggest that increased mutation strength on the hybrid background attenuates the previously reported male behavioral bias and unmasks genuinely strong female phenotypes once a higher mutational threshold is exceeded.

Brain volumes in *Chd8*^{+N2373K} and *Chd8*^{N2373K/N2373K} mice

Mouse behavioral changes can be driven by multiple factors that shape brain development and function. To investigate these influences, we evaluated both male and female *Chd8*^{+N2373K} and *Chd8*^{N2373K/N2373K} mice using assays that measured brain volume, cerebral blood flow, neuronal firing, synaptic transmission, and transcriptomic changes. CHD8 is known to regulate brain development and size, as evidenced by the macrocephaly commonly observed in autistic individuals with CHD8 mutations [1, 3, 4, 49, 52], although reduced expression of *Chd8* in mice gave mixed results in brain-size changes in gene dosage-sensitive manner [11, 13, 16, 17, 19, 20, 29, 31]. Additionally, the CHD8-N2373K mutation in the current study has been specifically linked to macrocephaly in both humans [4, 49] and mice [19].

We next used magnetic resonance imaging (MRI) to assess brain volumes in *Chd8*^{+N2373K} and *Chd8*^{N2373K/N2373K} mice. In *Chd8*^{+N2373K} mice, both males and females exhibited mixed trends in brain volume changes that did not reach significance (Fig. 3a, b), mirroring the lack of significant behavioral alterations (Fig. 2). In contrast, homozygous *Chd8*^{N2373K/N2373K} mice showed significant increases in brain volume across several regions (Fig. 3a, b). These volumetric increases were particularly prominent in mutant males, especially within cortical and hippocampal areas. Interestingly, while *Chd8*^{N2373K/N2373K} females also demonstrated increased volume in cortical regions, they showed decreasing tendencies in caudal regions, including the midbrain and hindbrain.

These results demonstrate that a homozygous *Chd8* mutation intensifies macrocephaly, thereby more clearly linking *Chd8* deficiency with increased brain volume. Specifically, both *Chd8*^{N2373K/N2373K} males and females exhibit similar increases in the cortical and hippocampal areas. However, they display divergent changes in the brain stem and hindbrain regions, with males showing increases and females showing decreases. It remains unclear whether these findings represent a gene dosage-dependent suppression of sexual dimorphism, particularly since *Chd8*^{+N2373K} mice did not exhibit significant alterations, even though the overall patterns of sexual dimorphism across gene dosages tended to be similar.

Cerebral blood volumes and flows in *Chd8*^{+N2373K} and *Chd8*^{N2373K/N2373K} mice

To determine whether altered brain volumes are associated with functional changes, we measured cerebral blood volume (CBV) and cerebral blood flow (CBF) using functional magnetic resonance imaging (fMRI) with a whole BOLD–dynamic susceptibility contrast (BOLD-DSC) protocol that employs brief hypoxia stimuli to elicit robust BOLD responses and provides estimates of

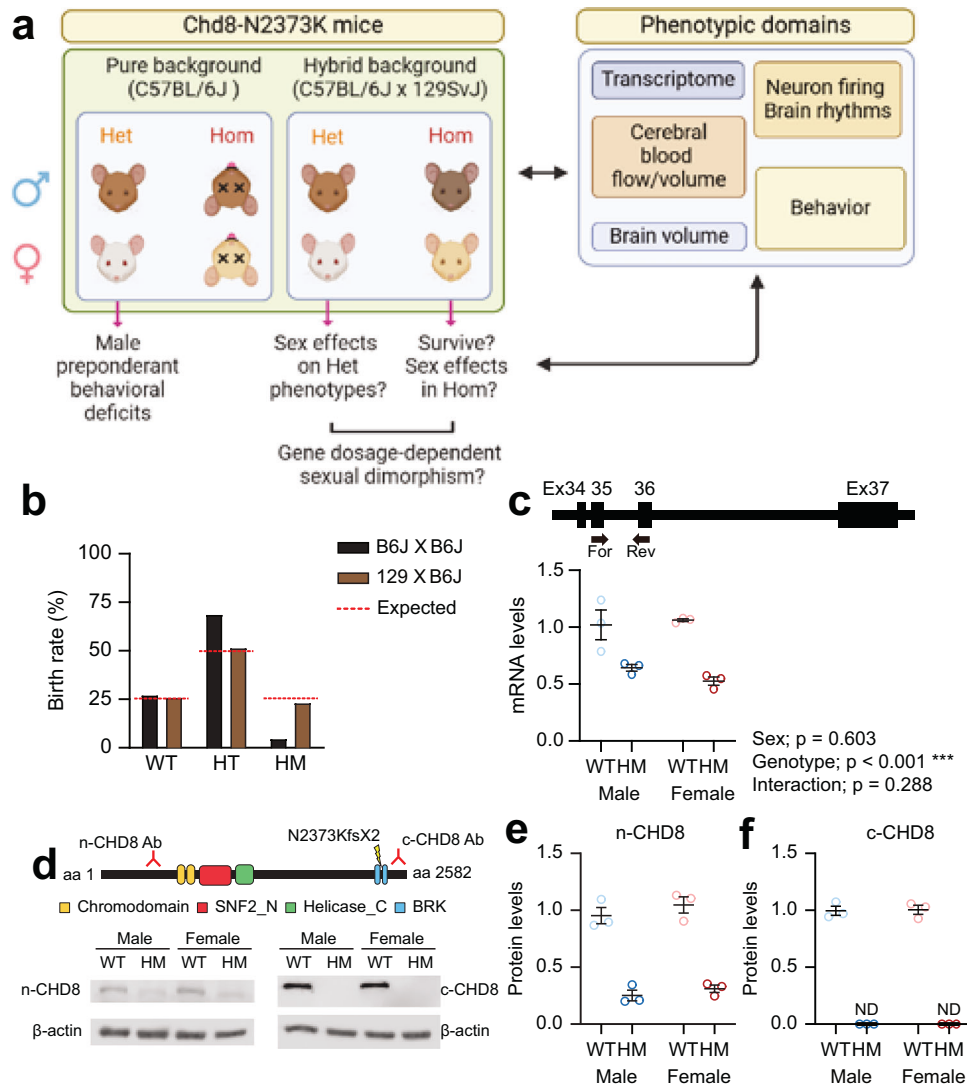


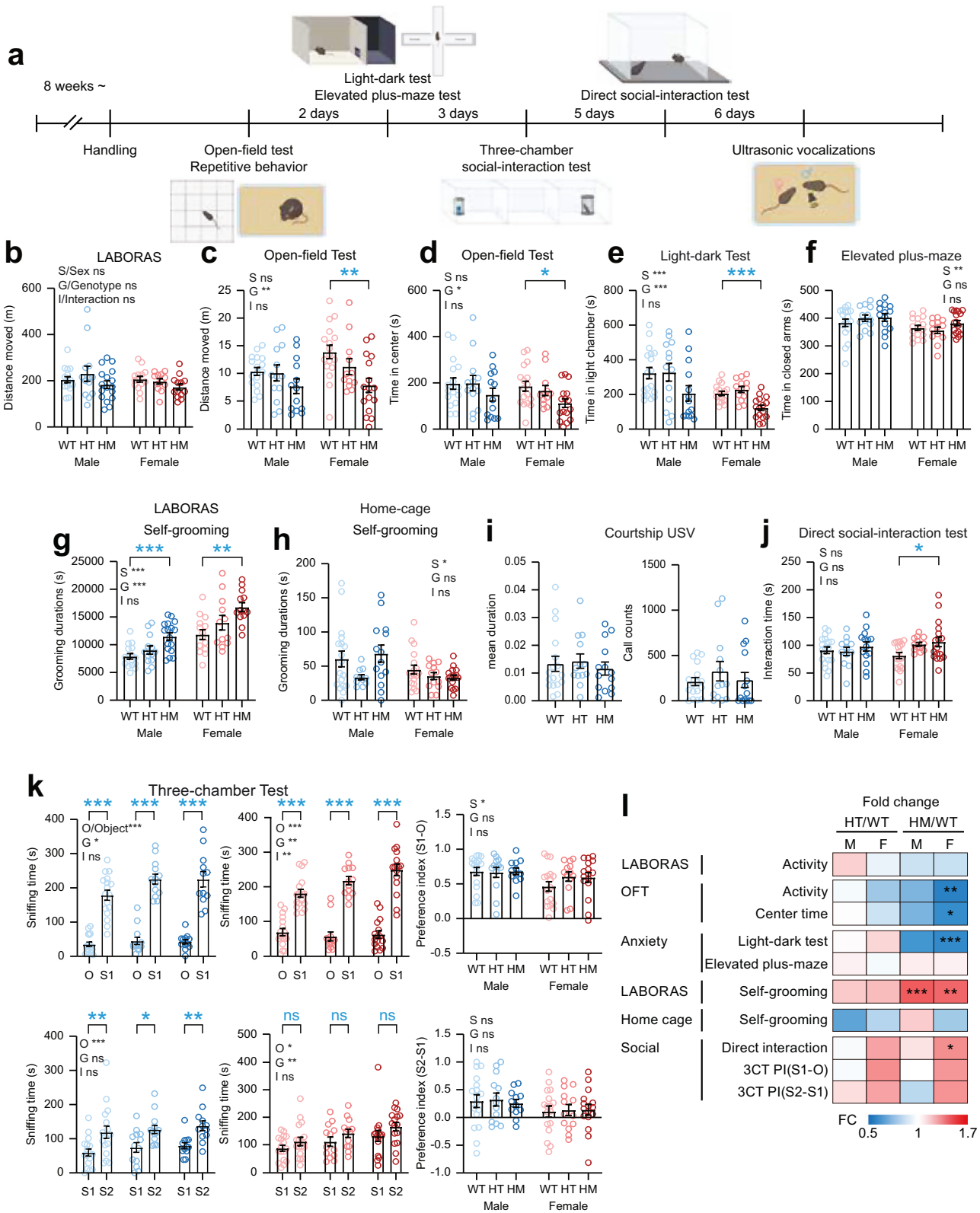
Fig. 1 **Generation of viable homozygous *Chd8*^{N2373K/N2373K} mice.** **a** Experimental design testing the FPE hypothesis using a *Chd8*-mutant (CHD8-N2372K) mouse model of ASD and manipulating the genetic dosage (heterozygous/Het and homozygous/Hom) and genetic background. In a pure genetic background (C57BL/6J), homozygous mutant mice are lethal. This lethality may be overcome by shifting the genetic background from a pure (C57BL6J) to hybrid (C57BL6J x 129/Sv) background in which we can compare various phenotypes (behavior, anatomical brain volume, functional cerebral blood flow/volume, neuronal firing, synaptic transmission, and transcriptome) from heterozygous and homozygous males and females. These data would enable to assess if a homozygous *Chd8* mutation can induce core ASD-like behaviors (i.e., self-grooming) and affects sexual dimorphic phenotypes in a gene deletion-dosage dependent manner. **b** Mendelian ratios of wild-type (WT), *Chd8*^{+/^{N2373K} (HT), and *Chd8*^{N2373K/N2373K} (HM) mice (~P7) in the pure (C57BL6/J) and hybrid (C57BL6/J x 129/Sv) genetic backgrounds. Note that the hybrid genetic background normalizes the Mendelian ratio. **c** Decreased levels of *Chd8* mRNAs (~50–60% of WT levels) in the brains of *Chd8*^{N2373K/N2373K} (HM) male and female mice (~P21), suggestive of nonsense-mediated decay, as determined by RT-qPCR. For/Rev indicates forward/reverse primers. **d–f** Decreased levels of CHD8 proteins (~20% of WT levels) in the brain of *Chd8*^{N2373K/N2373K} (HM) male and female mice (~2–3 months), as determined by immunoblot analysis of whole-brain lysates with antibodies targeting the N- and C-terminal regions of the protein, the positions of which are indicated above the protein domain diagram. Note that the C-terminal portion of the protein (~200 aa after the truncation point) is completely removed in *Chd8*^{N2373K/N2373K} mice, while the N-terminal portion of the protein before the truncation point is decreased to ~20% of WT levels, indicative of truncation-induced protein destabilization. SNF2_N, SNF2 family N-terminal domain; Helicase_C, Helicase conserved C-terminal domain; BRK, Brahma and Kismet domain.}

baseline CBV and CBF as proxies for resting perfusion and metabolic demand [53].

In *Chd8*^{+/^{N2373K} mice, males exhibited slight, non-significant decreases in CBV across several brain regions (Fig. 4a, b), while females showed mixed patterns of small increases and decreases, differing from the primarily decreasing trend seen in males. In contrast, both male and female *Chd8*^{N2373K/N2373K} mice displayed similar decreases in CBV in largely non-overlapping regions of male and female mutants, except for the retrosplenial cortex (Fig. 4a, b). Cerebral blood flow analyses produced similar patterns}

(Supplementary Fig. 3). As illustrated by the hypoxia-evoked CBV time courses in the hippocampus (Supplementary Fig. 4a), group differences were largely reflected in the magnitude of the peak response, whereas the overall temporal profile of the vascular response was preserved across genotypes and sexes, arguing against major alterations in vascular reactivity.

These results collectively suggest that a homozygous *Chd8* mutation leads to a more pronounced suppression of CBV and CBF. These CBV/CBF differences are unlikely to arise from systematic differences in systemic physiology or anesthetic depth,



as respiratory rates—an indicator of anesthetic depth—were comparable across groups during imaging. Due to the insignificant CBF differences observed in *Chd8^{+/N2373K}* mice, it remains unclear whether heightened mutational strength influences sexually dimorphic blood flow patterns. However, the contrasting trends in blood flow between *Chd8^{+/N2373K}* males and females

converge into a shared, significant decrease in both sexes in the homozygous mutants.

To investigate the relationship between regional CBV and MRI-derived brain volume (Fig. 4 vs. Figure 3), we performed correlation and ANCOVA analyses (Supplementary Fig. 4b–e). No significant associations were detected after correction for multiple

Fig. 2 Sexually dimorphic behavioral deficits in *Chd8*^{N2373K/N2373K} mice. **a** Schema of behavioral experiments for male and female *Chd8*^{+/N2373K} and *Chd8*^{N2373K/N2373K} mice (3–4.5 months). **b** Locomotor activity in the Laboras test (familiar environment) as shown by distance moved by male and female *Chd8*^{+/N2373K} and *Chd8*^{N2373K/N2373K} mice. Full details of the statistical analyses are provided in Supplementary Table 1. ($n = 16$ mice [M/male-WT/wild-type], 13 [M-HT/heterozygote], 17 [M-HM/homozygote], 14 [F/female-WT], 12 [F-HT], 13 [F-HM], two-way ANOVA). **c** Locomotor activity in the open-field test (novel environment) as shown by distance moved. ($n = 17$ [M-WT], 13 [M-HT], 13 [M-HM], 17 [F-WT], 12 [F-HT], 16 [F-HM]), two-way ANOVA, one-way ANOVA within sex [indicated by blue asterisks]). **d** Time spent in center during the open-field test, as a measure of anxiety-like behavior. ($n = 17$ [M-WT], 13 [M-HT], 13 [M-HM], 17 [F-WT], 12 [F-HT], 16 [F-HM]), two-way ANOVA, one-way ANOVA within sex). **e** Light-dark test for anxiety-like behavior. ($n = 18$ [M-WT], 13 [M-HT], 14 [M-HM], 17 [F-WT], 13 [F-HT], 16 [F-HM], two-way ANOVA, one-way ANOVA within sex). **f** Elevated plus-maze test for anxiety-like behavior. ($n = 18$ [M-WT], 13 [M-HT], 14 [M-HM], 17 [F-WT], 13 [F-HT], 17 [F-HM], two-way ANOVA within sex). **g** Self-grooming in Laboras cages. ($n = 16$ [M-WT], 13 [M-HT], 17 [M-HM], 14 [F-WT], 12 [F-HT], 13 [F-HM], two-way ANOVA, one-way ANOVA within sex). **h** Self-grooming in home cages. ($n = 18$ [M-WT], 11 [M-HT]; 14 [M-HM], 18 [F-WT], 13 [F-HT], 16 [F-HM], two-way ANOVA). **i** Courtship ultrasonic vocalizations (USVs). ($n = 17$ [M-WT], 13 [M-HT], 14 [M-HM], one-way ANOVA). **j** Direct social-interaction test. ($n = 18$ [M-WT], 12 [M-HT], 14 [M-HM], 18 [F-WT], 13 [F-HT], 17 [F-HM], two-way ANOVA, one-way ANOVA within sex). **k** Three-chamber social-interaction tests. S1, social target; O, object; S2, novel social target. Preference index: S1–O/S1 + O or S2–S1/S2 + S1. ($n = 17$ [M-WT], 13 [M-HT], 12 [M-HM], 17 [F-WT], 13 [F-HT], 16 [F-HM], two-way ANOVA, Student's t-test [S1 vs. O or S1 vs. S2], one-way ANOVA within sex). **l** Summary of the behavioral results from *Chd8*^{+/N2373K} and *Chd8*^{N2373K/N2373K} males and females. Red/blue colors indicate fold changes (increases/decreases) in HT/HM mice relative to WT mice, and stars indicate significant differences between HT/HM and WT mice (one-way ANOVA followed by Dunnett's test). Significance on two-way ANOVA is indicated as * (<0.05), ** (<0.01), *** (<0.001), or ns (not significant).

comparisons, although nominal negative correlations were observed only in prelimbic and retrosplenial cortices. Lastly, ANOVA versus ANCOVA comparisons including total brain volume and body weight as covariates (Supplementary Fig. 4e) yielded broadly similar patterns of group p values, indicating that regional CBV reductions are unlikely to be explained by variation in local regional volume, overall brain size, or body weight.

Neuronal firing and brain rhythms in *Chd8*^{+/N2373K} and *Chd8*^{N2373K/N2373K} mice

We next measured neuronal firing and local brain rhythms in various brain regions of male and female *Chd8*^{+/N2373K} and *Chd8*^{N2373K/N2373K} mice using Neuropixels probes under urethane anesthesia, which can stably measure high-density neuronal activity simultaneously in multiple brain regions of live animals [54]. Specifically, we measured neuronal activity in the cortex (retrosplenial or primary visual cortex, depending on the exact probe trajectory), hippocampus (CA1 and dentate gyrus/DG), and thalamus (lateral posterior and posterior thalamic regions) (Fig. 5a, b).

In *Chd8*^{+/N2373K} males under urethane, neuronal firing frequency increased by approximately 2–3-fold in the hippocampal dentate gyrus and thalamus, while *Chd8*^{+/N2373K} females did not show significant changes (Fig. 5c, d). Similarly, *Chd8*^{N2373K/N2373K} males exhibited increased neuronal firing in both the hippocampus (CA1 and DG) and thalamus, whereas homozygous mutant females remained unchanged. These results indicate that increased neuronal firing is a male-specific effect and is not affected by a stronger CHD8 mutation.

We next analyzed local field potentials (LFPs) to assess local brain rhythms (Supplementary Fig. 5a–d). In *Chd8*^{+/N2373K} males under urethane, LFP power showed increasing trends across multiple frequency bands (delta, theta, beta, low-gamma, and high-gamma) in the cortex, hippocampus (CA1/DG), and thalamus, whereas *Chd8*^{+/N2373K} females exhibited mixed trends (Fig. 5e). However, none of these changes reached statistical significance. In contrast, *Chd8*^{N2373K/N2373K} mice displayed decreasing trends in LFP power in both sexes with some male regions (e.g., DG) reaching significance, differing from the patterns seen in heterozygous mice (Fig. 5e).

In a separate set of head-fixed awake recordings targeting the same cortical, hippocampal, and thalamic regions from *Chd8*^{N2373K/N2373K} mice, male-specific increases in neuronal firing was observed in a subset of the brain regions (DG and thalamus but not CA1) (Fig. 5f), being partly similar to the results from anesthetized *Chd8*^{N2373K/N2373K} mice. Notably, the cortex displayed similar decreases in neuronal firing in male and female mutants, while the CA1 region showed a female (not male)-specific increase. These results indicate brain region-differential effects of urethane on neuronal firing. In addition, the switch in directionality from increased (anesthetized) to decreased (awake) cortical

firing, and the emergence of a female-specific CA1 increase only in awake mice, likely reflects the well-known modulatory effects of urethane on excitatory and inhibitory neurotransmission [55, 56], which can differentially mask or unmask region- and circuit-specific firing alterations depending on the local balance of excitation and inhibition [57–59]. Indeed, cortical responses in awake mice are dominated by inhibition and are more temporally restricted than under urethane anesthesia, where prolonged excitatory drive predominates [60], consistent with a state-dependent shift in excitation–inhibition balance underlying the observed directionality switch.

When LFPs were analyzed in awake mice, LFP powers were tended to decrease in the thalamus of both sexes and in male (but not female) cortex, CA1, and DG (Fig. 5g; Supplementary Fig. 6), being qualitatively similar to the results from anesthetized mice, although these results were largely statistically insignificant. Overall, these findings indicate that the homozygous *Chd8*^{N2373K/N2373K} mutation does not further elevate neuronal firing as compared with the heterozygous *Chd8*^{+/N2373K} mutation under anesthesia, being already pronounced in heterozygous males especially in the DG and thalamus, as further supported by the awake-mouse results. Whether gene dosage suppresses sexual dimorphism in LFP remains unclear due to the largely insignificant LFP changes in heterozygous and homozygous mice under anesthesia, although a trend toward suppression is apparent especially in the thalamus.

Synaptic transmission in *Chd8*^{+/N2373K} and *Chd8*^{N2373K/N2373K} mice

We next assessed excitatory and inhibitory synaptic transmission in hippocampal CA1 pyramidal neurons from *Chd8*^{+/N2373K} and *Chd8*^{N2373K/N2373K} mice, given that prior work in a pure genetic background reported female-specific increases in inhibitory transmission in *Chd8*^{+/N2373K} mice [19].

On the hybrid background used here, *Chd8*^{+/N2373K} males showed no detectable changes in miniature excitatory postsynaptic currents (mEPSCs), while *Chd8*^{+/N2373K} females showed a non-significant tendency toward reduced mEPSC frequency (Supplementary Fig. 7a). In addition, miniature inhibitory postsynaptic currents (mIPSCs) remained unchanged in both sexes of *Chd8*^{+/N2373K} mice (Supplementary Fig. 7b), differing from earlier findings in a pure background [19], which is likely to be caused by a change in the genetic background.

In homozygous *Chd8*^{N2373K/N2373K} mice, mEPSCs and mIPSCs were unaltered in both sexes (Supplementary Fig. 7a, b). Moreover, spontaneous excitatory and inhibitory currents (sEPSCs and sIPSCs) were unaltered in all groups (Supplementary Fig. 7c, d).

In additional recordings from layer 2/3 and layer 5 pyramidal neurons in the medial prefrontal cortex (mPFC) and from dorsal striatal neurons, sEPSC and sIPSC properties were generally normal in

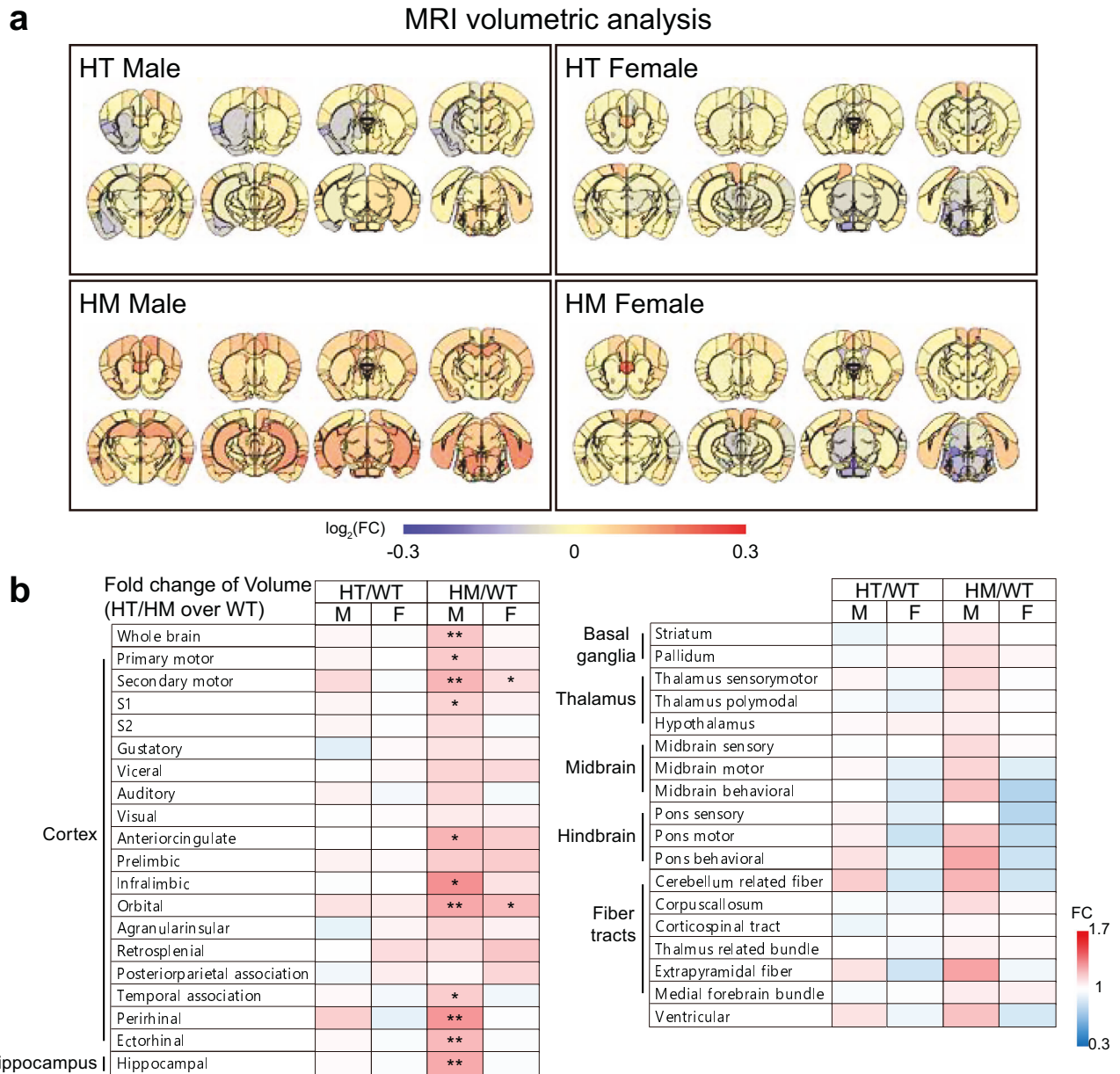


Fig. 3 Brain volumes in $Chd8^{+/N2373K}$ and $Chd8^{N2373K/N2373K}$ males and females. **a** MRI analysis of alterations in anatomical brain volumes in $Chd8^{+/N2373K}$ and $Chd8^{N2373K/N2373K}$ male and female mice (~6–8 months). Red/blue colors indicate fold changes (increases/decreases) in HT/HM relative to WT mice. ($n = 5$ mice [M-WT], 5 [M-HT]; 5 [M-HM], 5 [F-WT], 5 [F-HT], 5 [F-HM]). **b** Color-coded display of the altered anatomical brain volumes in the different brain regions shown in (a). Stars indicate significant differences between HT/HM mice and WT mice within males/females (one-way ANOVA with Dunnett's test). The whole brain value represents the total brain volume calculated as the sum of all the indicated brain region volumes. Significance is indicated as * (<0.05), ** (<0.01), *** (<0.001), or ns (not significant).

$Chd8^{N2373K/N2373K}$ mice, with the exception of an increase in sIPSC frequency in layer 5 pyramidal neurons (Supplementary Fig. 8a–f).

Collectively, these results indicate that the heterozygous $Chd8$ mutation does not affect synaptic properties in the hippocampus of mice on the hybrid background, underscoring, together with previous results from a pure background with female-specific inhibitory synaptic increases [19], that genetic background strongly shapes the expression of synaptic changes. The present data further demonstrate that the homozygous $Chd8$ mutation does not alter baseline excitatory or inhibitory synaptic transmission in the hippocampus, mPFC, or striatum. As such, these findings do not address whether increased $Chd8$ mutational strength intensifies synaptic phenotypes or contributes to synaptic sexual dimorphism.

Transcriptomic changes in $Chd8^{+/N2373K}$ and $Chd8^{N2373K/N2373K}$ mice

To explore molecular mechanisms associated with the phenotypic changes in $Chd8^{+/N2373K}$ and $Chd8^{N2373K/N2373K}$ males and females, we next performed transcriptomic analyses at three postnatal stages (P0, P25, and P56) using whole-brain samples and in adults across three regions (hippocampus, cortex, and striatum) (Fig. 6; Supplementary Table 2). Our RNA-Seq analyses mainly involved two approaches; analyses of differentially expressed genes (DEGs) and gene set enrichment analysis (GSEA) [61]. The latter used ASD-related gene sets (DEG Up Voineagu, Co-Exp Up M16 Voineagu, DEG Down Voineagu, Co-Exp Down M12 Voineagu) [62, 63], ASD-risk gene sets (SFARI Genes [All, High-confidence] [64], FMRP Targets [63, 65], DeNovoMissense [63, 66], DeNovoVariants

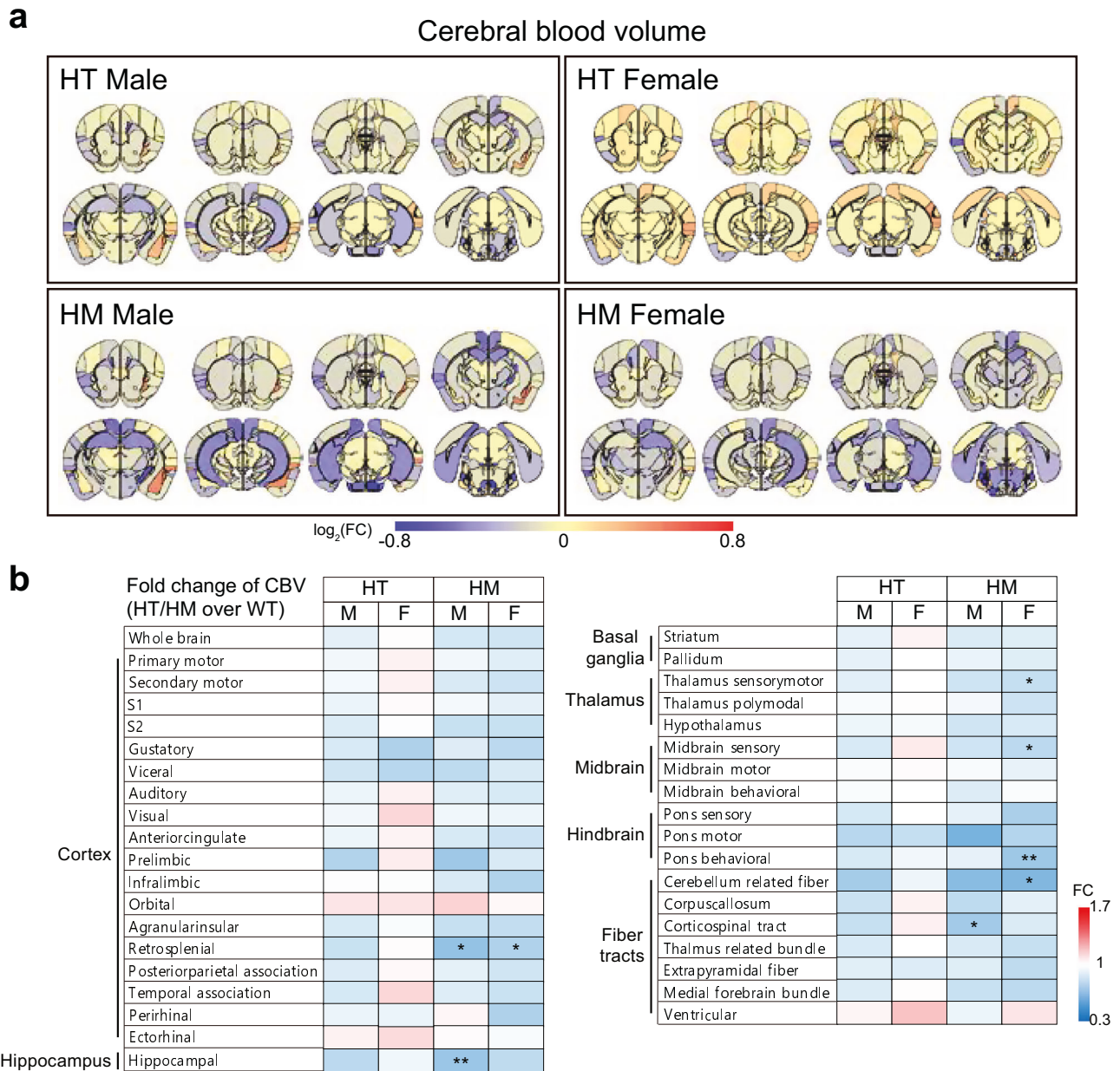


Fig. 4 Cerebral blood volumes in $Chd8^{+/N2373K}$ and $Chd8^{N2373K/N2373K}$ males and females. **a** Blood volumes in different brain regions of $Chd8^{+/N2373K}$ and $Chd8^{N2373K/N2373K}$ male and female mice (~4–5 months), as measured by fMRI responding to 5-sec nitrogen stimulus under anesthesia (isoflurane). Red/blue colors indicate fold changes (increases/decreases) in HT/HM relative to WT mice. ($n = 5$ mice [M-WT], 5 [M-HT]; 5 [M-HM], 5 [F-WT], 5 [F-HT], 5 [F-HM]). **b** Color-coded display of the altered cerebral blood volumes in the different brain regions shown in (a). Stars indicate significant differences between HT/HM mice and WT mice within males/females (one-way ANOVA with Dunnett's test). The whole brain value represents the average blood volume across all the indicated brain regions. Significance is indicated as * (<0.05), ** (<0.01), *** (<0.001), or ns (not significant).

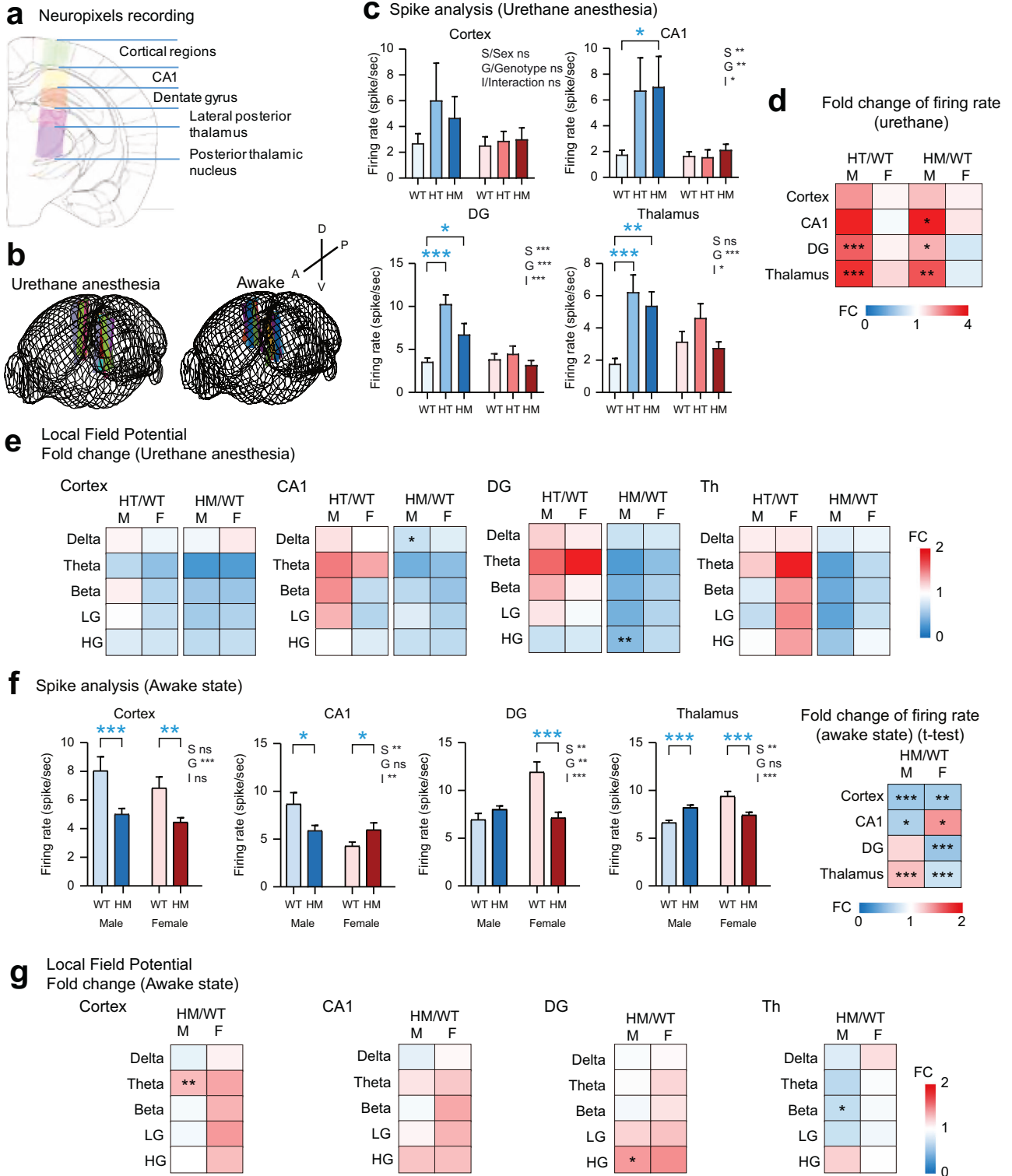
[63, 66], and AutismKB [67, 68]), and biological function-related gene sets in the Molecular Signature Database (MSigDB).

At P0, only small numbers of DEGs were observed in $Chd8^{+/N2373K}$ mice without apparent difference in males and females (Fig. 6a; Supplementary Table 3 [all DEG results]). In $Chd8^{N2373K/N2373K}$ mice, similar results were also observed, although DEG numbers were slightly increased. This suggests that gene deletion dosage increases DEG numbers but does not affect sexual dimorphism.

In the GSEA for P0, $Chd8^{+/N2373K}$ and $Chd8^{N2373K/N2373K}$ males and females showed largely similar changes in ASD-related/risk gene sets, with the $Chd8^{N2373K/N2373K}$ mice showing slightly

stronger ASD-like patterns; i.e., $Chd8^{N2373K/N2373K}$ males and females showing stronger ASD-like patterns such as stronger upregulation of ASD-related genes (DEG Up and Co-Exp Up) and stronger downregulation of ASD-related genes (DEG Down, Co-Exp Down) and ASD-risk genes (i.e., SFARI) (Fig. 6b; Supplementary Table 4 [all GSEA results]).

At P25, $Chd8^{+/N2373K}$ males showed stronger changes in DEGs (both up and down) as compared with $Chd8^{+/N2373K}$ females (Fig. 6a). Intriguingly, in $Chd8^{N2373K/N2373K}$ mice, DEG numbers being similar in males and females, suggestive of gene dosage-dependent suppression of sexual dimorphism in DEG number. Accordingly, the GSEA results from $Chd8^{+/N2373K}$ mice showed



stronger 'reverse-ASD' patterns (changes opposite to those observed in ASD) in females relative to males; i.e., downregulation of Co-Exp UP genes and upregulation of most ASD-risk gene sets (SFARI and FMRP Targets) (Fig. 6b). However, this strong reverse-ASD pattern in *Chd8*^{+/N2373K} females was changed to ASD-like patterns in *Chd8*^{N2373K/N2373K} females, partly similar to the male pattern, again suggesting gene dosage-dependent suppression of sexual dimorphism.

At P56, similar gene dosage-dependent suppression of sexual dimorphism was observed in both DEG numbers and GSEA results from *Chd8*^{+/N2373K} and *Chd8*^{N2373K/N2373K} mice (Fig. 6a, b), indicating that gene dosage-dependent suppression of sexual dimorphism is detectable at ~P25 and persists into adulthood.

In DEG analyses for different brain regions (hippocampus, cortex, and striatum) at P56, brain region-specific changes were

Fig. 5 **Neuronal firing and brain rhythms in $Chd8^{+/N2373K}$ and $Chd8^{N2373K/N2373K}$ males and females.** **a** Schema of Neuropixels recording of neuronal firing in multiple brain regions of $Chd8^{+/N2373K}$ and $Chd8^{N2373K/N2373K}$ males and females (9–16 weeks), including the cortex (retrosplenial and visual), hippocampus (CA1 and dentate gyrus/DG), and thalamus (lateral posterior and posterior thalamic). Scale bar, 1 mm. **b** Post-hoc histological 3D reconstruction of Neuropixels probe tracks, with different colors representing individual animals. Tracks are shown for the urethane anesthesia experiment (left) and the head-fixed awake experiment (right). **c** Neuronal firing rates in multiple brain regions (cortex, hippocampal CA1 and DG, and thalamus), measured by Neuropixels recordings under urethane anesthesia. (Cortex, $n = 28$ neurons from 9 mice [M-WT], 22, 8 [M-HT], 15, 9 [M-HM], 27, 5 [F-WT], 26, 5 [F-HT], 20, 5 [F-HM]; CA1, 40, 9 [M-WT], 21, 8 [M-HT], 24, 9 [M-HM], 48, 5 [F-WT], 23, 5 [F-HT], 46, 5 [F-HM]; DG 185, 9 [M-WT], 125, 8 [M-HT], 68, 9 [M-HM], 76, 5 [F-WT], 66, 5 [F-HT], 122, 5 [F-HM]; Th, 100, 9 [M-WT], 116, 8 [M-HT], 136, 9 [M-HM], 121, 5 [F-WT], 98, 5 [F-HT], 205, 5 [F-HM], two-way ANOVA, one-way ANOVA [within-sex comparison of WT, HT, and HM]). **d** Ratios of neuronal firing rates (HT/WT and HM/WT) in multiple brain regions (cortex, CA1, DG, and thalamus; urethane). Red/blue colors indicate fold changes (increases/decreases) in HT/HM mice relative to WT mice, and stars indicate significant differences between HT/HM and WT mice within males/females. ($n = 9$ [M-WT], 8 [M-HT], 9 [M-HM], 5 [F-WT], 5 [F-HT], and 9 [F-HM], one-way ANOVA with Dunnett's test). **e** Ratios of local rhythms (HT/WT and HM/WT) in multiple brain regions (cortex, CA1, DG, and cortex) of $Chd8^{+/N2373K}$ and $Chd8^{N2373K/N2373K}$ males and females (9–16 weeks; urethane). Red/blue colors indicate fold changes (increases/decreases) in HT/HM mice relative to WT mice, and stars indicate significant differences between HT/HM and WT mice (one-way ANOVA with Dunnett's test). ($n = 9$ [M-WT], 8 [M-HT], 8 [M-HM], 5 [F-WT], 6 [F-HT], and 8 [F-HM], one-way ANOVA with Dunnett's test). **f** Awake-state neuronal firing rates in multiple brain regions (cortex, CA1, DG, and thalamus) and ratios of neuronal firing rates (HM/WT). (Firing rates: Cortex, 106 neurons from 3 mice [M-WT], 212, 3 [M-HM], 154, 4 [F-WT], 257, 3 [F-HM]; CA1, 62, 3 [M-WT], 131, 3 [M-HM], 211, 4 [F-WT], 116, 3 [F-HM]; DG, 108, 3 [M-WT], 202, 3 [M-HM], 153, 4 [F-WT], 159, 3 [F-HM]; Th, 671, 3 [M-WT], 777, 3 [M-HM], 549, 4 [F-WT], 760, 3 [F-HM], one-way ANOVA with Dunnett's test; Ratios of firing rates: $n = 6$ hemispheres from 3 mice [M-WT], 6, 3 [M-HM], 6, 3 [F-WT], and 6, 3 [F-HM], two-way ANOVA, unpaired t-test [within-sex comparison of WT and HM]). **g** Awake-state ratios of local rhythms (HM/WT) in multiple brain regions (cortex, CA1, DG, and cortex) of $Chd8^{+/N2373K}$ and $Chd8^{N2373K/N2373K}$ males and females (9–16 weeks). (Cortex, $n = 4$ hemispheres from 3 mice [M-WT], 3, 3 [M-HM], 5, 4 [F-WT], 4, 3 [F-HM]; CA1, 4, 3 [M-WT], 3, 3 [M-HM], 7, 4 [F-WT], 4, 3 [F-HM]; DG, 4, 3 [M-WT], 3, 3 [M-HM], 6, 4 [F-WT], 4, 3 [F-HM]; Th, 4, 3 [M-WT], 3, 3 [M-HM], 6, 4 [F-WT], 4, 3 [F-HM], two-way ANOVA, unpaired t-test [within-sex comparison of WT and HM]). Significance is indicated as * (<0.05), ** (<0.01), *** (<0.001), or ns (not significant).

observed. The hippocampus and cortex, but not the striatum, showed DEG patterns that are similarly robust in $Chd8^{N2373K/N2373K}$ males and females (Fig. 6c), mirroring patterns observed in the whole brain. GSEA analyses for ASD-related/risk gene sets revealed that the hippocampus and striatum, but not the cortex, showed stronger gene dosage-dependent suppression of sexual dimorphism (Fig. 6d), partially aligning with results from both whole-brain analyses and DEG findings.

Collectively, these findings indicate that a homozygous $Chd8$ mutation amplifies transcriptomic alterations, as evidenced by a higher number of DEGs and more pronounced ASD-like GSEA changes, particularly at postnatal day 56 and in the striatum. Moreover, gene dosage-dependent suppression of sexual dimorphism emerges in a developmental stage- and brain region-specific manner, again most notably at P56 (in both DEG and GSEA analyses) and within the striatum (via GSEA). For example, the robust reverse-ASD pattern observed in $Chd8^{+/N2373K}$ females across the whole brain shifts to an ASD-like pattern shared by both male and female $Chd8^{N2373K/N2373K}$ mice, with a similar transition noted in the striatum at P56.

Biological functions linked to transcriptomic changes in $Chd8^{+/N2373K}$ and $Chd8^{N2373K/N2373K}$ mice

To better understand the biological basis of the abovementioned transcriptomic changes (i.e., ASD-related/risk gene expressions and gene dosage-dependent suppression of sexual dimorphism), we performed GSEA using biological function-related gene sets in the gene ontology (GO) cellular component/CC and biological process/BP domains (summarized Fig. 6e; see Supplementary Figs. 9–12 for details; Supplementary Table 4).

At P0, robust ASD-like transcriptomic changes were observed in the whole brains of both $Chd8^{+/N2373K}$ and $Chd8^{N2373K/N2373K}$ males and females (Fig. 6b). Consistent upregulation of ribosomal and proteasomal genes was evident across all genotypes and sexes (Fig. 6e; Supplementary Figs. 9–12). Notably, while mitochondrial upregulation was present in $Chd8^{+/N2373K}$ mice, this shifted to synaptic downregulation in $Chd8^{N2373K/N2373K}$ mice. In addition, distinct male-only and female-only gene regulations were identified. These findings indicate that at P0, gene regulation is influenced by both genotype and sex, exhibiting both shared and unique patterns.

At P25, $Chd8^{+/N2373K}$ females exhibit pronounced reverse-ASD patterns across the whole brain (Fig. 6b). Notably, these females

display unique changes; synaptic upregulation paired with mitochondrial and splicing downregulation (Fig. 6e; Supplementary Figs. 9–12). These alterations may contribute to female neuroprotection, aligning with previous reports of robust, female-specific increases in inhibitory synaptic transmission in $Chd8^{+/N2373K}$ females on a pure genetic background [19].

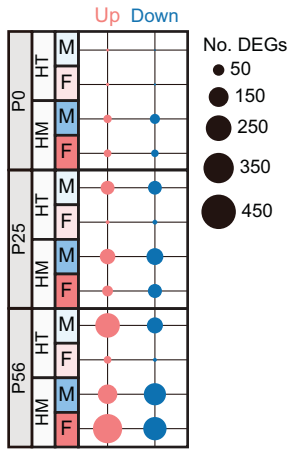
At P56, $Chd8^{N2373K/N2373K}$ mice exhibit pronounced ASD-like transcriptomic patterns across the whole brain, whereas $Chd8^{+/N2373K}$ mice of both sexes did not display these alterations (Fig. 6b). Alongside the observed age-dependent decline in ASD-related/risk gene expression from P0 to P25 and P56, this suggests a spontaneous normalization of ASD-related gene expression in $Chd8^{+/N2373K}$ mice, which is consistent with their largely normal behavioral phenotypes. In contrast, biological changes remain prominent in $Chd8^{N2373K/N2373K}$ mice, characterized by a shared upregulation of ribosomal genes and sex-specific alterations; namely, synaptic downregulation in males and splicing and mitochondrial downregulations in females (Fig. 6e; Supplementary Figs. 9–12).

In specific brain regions, particularly the hippocampus and striatum in $Chd8^{N2373K/N2373K}$ males and females, which show shared ASD-like changes (Fig. 6d), shared biological alterations were observed in $Chd8^{N2373K/N2373K}$ mice but not in $Chd8^{+/N2373K}$ mice; downregulations of ribosomal and synaptic genes were evident in the hippocampus and striatum, respectively (Fig. 6e).

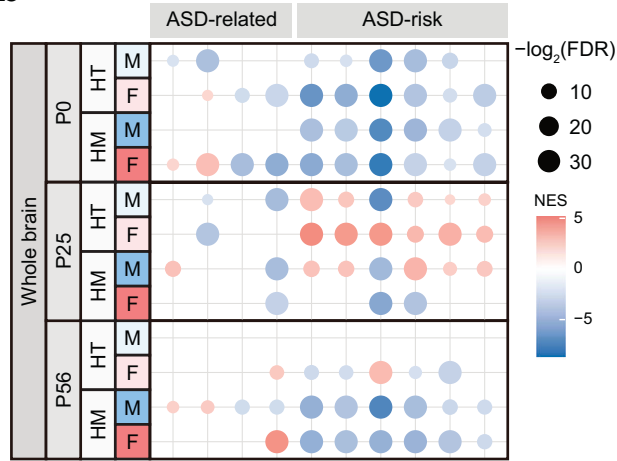
Notably, the downregulated mitochondrial and splicing gene sets unique to P25 $Chd8^{+/N2373K}$ females (whole brain) were no longer detectable in P56 $Chd8^{+/N2373K}$ females, but emerged in P56 $Chd8^{N2373K/N2373K}$ females as upregulated gene sets (Fig. 6e). These opposite changes might underlie the contrasting female-protective and female-susceptible phenotypes/behaviors at P25 and P56 (e.g., reverse-ASD and ASD-like transcriptomes, respectively; Fig. 6b). To determine whether these contrasting changes involve a similar set of synaptic genes, we conducted leading edge analyses [61]. The results indicated that many shared splicing and mitochondrial genes (i.e., Snrpg [small nuclear ribonucleoprotein G] and Txnl4a [thioredoxin-like protein 4 A]); key components of the spliceosome) were involved in the opposite changes (Supplementary Fig. 13).

On a similar note, the synaptic upregulation in P25 $Chd8^{+/N2373K}$ females (whole brain) contrasted with the strong synaptic downregulation shared in P56 $Chd8^{N2373K/N2373K}$ males and females (striatum). Our results, however, indicated that distinct synaptic genes were involved in these cases; i.e., Grin2a,

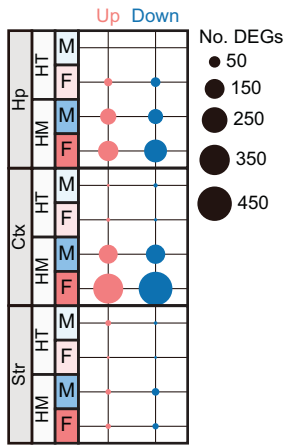
a DEG counts



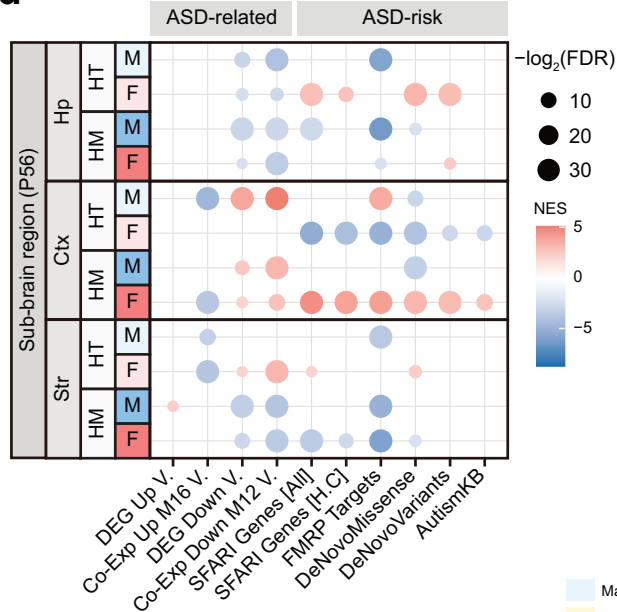
b GSEA results



c DEG counts



d GSEA results



e GSEA Cellular Component

| | P0 | P25 | P56 |
|----|---|--|---|
| HT | Mitochondria Ribosome Proteasome | Synapse ECM | Chromosome Ribosome Synapse Splicing Mitochondria |
| HM | Mitochondria Synapse Ribosome Proteasome | Splicing Chromosome | Ribosome Chromosome Synapse Ribosome Splicing Mitochondria |
| | Hippocampus | Cortex | Striatum |
| HT | Mitochondria Ribosome | Vesicle Mitochondria Synapse Proteasome | Synapse Mitochondria Ribosome |
| HM | Ribosome | Synapse Ribo-Mito | Ribosome Chromosome Synapse Mitochondria Transcription |

Grin2b, and Shisa6 (regulators of NMDARs and AMPARs) in P25 *Chd8*^{+/*N2373K*} females and Ntn2 and Lfn2 (synaptic adhesion molecules) in P56 *Chd8*^{*N2373K/N2373K*} mice (Supplementary Fig. 14), likely because we compared two different brain regions (whole brain vs. striatum).

Collectively, these results indicate that a homozygous *Chd8* mutation amplifies biological changes, most notably at P56 in the whole brain and striatum, as reflected by an increased number of gene-set clusters. Increased *Chd8* mutation strength appears to suppress, and in specific gene sets partially reverse, sexual

Fig. 6 Transcriptomic changes in $Chd8^{+/N2373K}$ and $Chd8^{N2373K/N2373K}$ males and females. **a, b** Differentially expressed gene (DEG; a) and Gene set enrichment analysis (GSEA; b) analyses of transcriptomes from whole brains of $Chd8^{+/N2373K}$ and $Chd8^{N2373K/N2373K}$ males and females at P0, P25, and P56. The GSEA used ASD-related sets (DEG Up Voineagu, Co-Exp Up M16 Voineagu, DEG Down Voineagu, Co-Exp Down M12 Voineagu) and ASD-risk gene sets (SFARI Genes [All, High-confidence], FMRP Targets, DeNovoMissense, DeNovoVariants, and AutismKB). Up/Down, up/down regulations; P0/25/56, postnatal day 0/25/56; FDR, false discovery rate; NES, normalized enrichment score. ($n = 5$ mice [WT-male-P0], 5 [WT-female-P0], 5 [HT-male-P0], 5 [HT-female-P0], 5 [HM-male-P0], 5 [HM-female-P0]), 5 [WT-male-P25], 5 [WT-female-P25], 5 [HT-male-P25], 5 [HT-female-P25], 5 [HM-male-P25], 5 [HM-female-P25]), 5 [WT-male-P56], 5 [WT-female-P56], 5 [HT-male-P56], 5 [HT-female-P56], 5 [HM-male-P56], 5 [HM-female-P56], FDR < 0.05). **c, d** DEG and GSEA analyses of transcriptomes from three different brain regions (hippocampus/Hp, cortex/Ctx, and striatum/Str) of $Chd8^{+/N2373K}$ and $Chd8^{N2373K/N2373K}$ males and females at P56. ($n = 5$ [WT-male-Hp], 5 [WT-female-Hp], 5 [HT-male-Hp], 5 [HT-female-Hp], 5 [HM-male-Hp], 5 [HM-female-Hp]), 5 [WT-male-Ctx], 5 [WT-female-Ctx], 5 [HT-male-Ctx], 5 [HT-female-Ctx], 5 [HM-male-Ctx], 5 [HM-female-Ctx]), 5 [WT-male-Str], 5 [WT-female-Str], 5 [HT-male-Str], 5 [HT-female-Str], 5 [HM-male-Str], 5 [HM-female-Str], FDR < 0.05). **e** A summary of the biological functions associated with the transcriptomic changes observed in $Chd8^{+/N2373K}$ and $Chd8^{N2373K/N2373K}$ mice across both sexes. These functions highlight the effects induced by increased gene deletion dosage and reveal both shared and distinct changes between males and females (see Supplementary Figs. 8–11 for details). For simplicity, only the GSEA results in the Gene Ontology—Cellular Component (GO-CC) domain are summarized. Male-only, female-only, and male/female-shared changes are indicated in light blue, pink, and yellow backgrounds, respectively, while up- and downregulated gene sets are marked in red and blue.

dimorphism in biological functions. For example, the synaptic upregulation along with the splicing and mitochondrial down-regulations that are uniquely observed in P25 $Chd8^{+/N2373K}$ females (but not in males) are either eliminated (synapse) or reversed (splicing and mitochondria) in P56 $Chd8^{N2373K/N2373K}$ females.

DISCUSSION

By utilizing a hybrid genetic background to circumvent the lethality typically associated with homozygous $Chd8$ mutations, we generated both heterozygous ($Chd8^{+/N2373K}$) and homozygous ($Chd8^{N2373K/N2373K}$) mice, enabling a systematic comparison of gene dosage effects on phenotypic severity and male-female phenotypes. Our results indicate that increasing the severity of $Chd8$ mutations intensifies ASD-related phenotypes and attenuates male-female behavioral differences while reducing sexually dimorphic patterns across several neurobiological domains (i.e., cerebral blood flow, brain rhythms, and transcriptomes).

Behaviorally, $Chd8^{+/N2373K}$ mice on a pure genetic background display predominantly male-biased deficits [19], whereas in the hybrid background, $Chd8^{N2373K/N2373K}$ mice exhibit either male-female shared repetitive behaviors or even female-preponderant deficits. This shift likely reflects the combined influence of the altered genetic background and the increased mutation strength. Although direct behavioral comparisons in the hybrid background did not conclusively demonstrate that increased mutational strength suppresses sexual dimorphism, primarily because $Chd8^{+/N2373K}$ mice showed minimal behavioral changes, other phenotypic assessments (including brain volume, cerebral blood flow, neuronal firing, synaptic transmission, and transcriptomic profiles) strongly indicate that a higher mutation strength attenuates sexually dimorphic traits. These findings underscore mutation strength as a critical factor in modulating sex differences.

A potential framework for interpreting these results is the female protective effects (FPE) hypothesis, which posits that females require a higher mutational threshold to manifest neurodevelopmental disorders such as ASD [69–75]. Although the FPE hypothesis offers intuitive and testable predictions, direct neurobiological evidence from animal models of ASD and other neurodevelopmental disorders has been limited. While many mouse models of ASD display sexually dimorphic phenotypes, the underlying mechanisms remain elusive [63, 75–84]. Our current results, together with the previous report [19], provides evidence that can be aligned with the FPE hypothesis: heterozygous mutants (pure genetic background) frequently exhibit pronounced sex differences, whereas homozygous mutants (hybrid genetic background) display more convergent phenotypes. This suggests that once the genetic insult surpasses a female-specific protective threshold, female phenotypes become comparable to, or even more severe than, those in males (i.e.,

equally robust self-grooming or even stronger other behavioral deficits in $Chd8^{N2373K/N2373K}$ females). FPEs are thought to contribute to the marked sex ratios observed in various neurodevelopmental disorders, including ASD [69–74, 78–83], ADHD [85, 86], and schizophrenia [87, 88]. Moreover, CHD8 is implicated in ASD [1–7] and many other neurodevelopmental conditions, such as intellectual disability, developmental delay, ADHD, and schizophrenia [8, 9]. Thus, our findings may offer broader insights into the mechanisms underlying sexual dimorphism across multiple neurodevelopmental disorders.

Our analyses of brain anatomy and cerebral blood flow offer further insights into CHD8's role in brain development and function. Homozygous $Chd8^{N2373K/N2373K}$ mice exhibit increased brain volumes compared to heterozygous $Chd8^{+/N2373K}$ mice, suggesting that a strong reduction in $Chd8$ expression drives macrocephaly, a finding consistent with previous studies in mice expressing approximately 35% of wild-type CHD8 levels [31]. Regarding sex differences, both mutant males and females show similar increases in the cortical and hippocampal regions. However, they diverge in the brain stem and hindbrain regions, with males displaying increases and females showing decreases. In contrast, cerebral blood flow is similarly reduced across all brain regions in both sexes of $Chd8^{N2373K/N2373K}$ mice. This suggest that there is a disconnect between the anatomical macrocephaly induced by the $Chd8$ mutation and functional brain activity and that cerebral blood flow shows a stronger gene dose-dependent suppression of sexual dimorphism than brain volume.

Data on neuronal firing and synaptic transmission provide further insight into the functional impact of $Chd8$ mutations. Under urethane anesthesia, both heterozygous ($Chd8^{+/N2373K}$) and homozygous ($Chd8^{N2373K/N2373K}$) males show similarly elevated neuronal firing across multiple regions, indicating that stronger mutation does not further increase this abnormality, whereas females show minimal firing changes but display LFP power reductions that resemble those in males, consistent with attenuated sexual dimorphism in brain rhythms. In awake recordings, the male-specific increase in firing is again apparent in DG and thalamus of $Chd8^{N2373K/N2373K}$ mice, while both sexes show reduced firing in the cortex and a shared reduction in thalamic LFP power, suggesting a brain region-specific suppression of sexual dimorphism, although most LFP changes did not reach statistical significance in either anesthetized or awake conditions.

Our transcriptomic analyses further illuminate CHD8 function by extending previous findings on age- and brain region-specific differences in $Chd8$ -mutant mice [13, 16, 20, 28, 40, 89]. Moreover, increased CHD8 mutation strength suppresses sexually dimorphic transcriptomic patterns, as revealed by both DEG and GSEA analyses. These effects vary by developmental stage and brain region, with the most pronounced changes at P56 and in the striatum. For example, the synaptic gene sets uniquely upregulated in P25 $Chd8^{+/N2373K}$ females (whole brain) are no longer

detectable at P56 and instead appear as downregulated gene sets in P56 *Chd8*^{+/N2373K} males and females (striatum), suggesting a loss of female-specific synaptic protective effects. Likewise, the mitochondrial and splicing gene sets downregulated at P25 in *Chd8*^{+/N2373K} females (whole brain) disappear by P56 but re-emerge as upregulated in P56 *Chd8*^{N2373K/N2373K} females (whole brain), indicating that these pathways may contribute to the developmental shift from female protection to susceptibility.

Despite these robust findings, some limitations merit consideration. While our transcriptomic analyses have identified candidate biological functions and genes, they do not establish causal relationships between the diverse phenotypic changes observed, spanning behavior, brain structure, cerebral blood flow, neuronal firing, and synaptic transmission. Moreover, the development and suppression of sexually dimorphic phenotypes are complex processes influenced by developmental stage and brain region, complicating the establishment of definitive correlations across different domains.

In summary, our findings demonstrate that a homozygous *Chd8* mutation in mice elicits robust ASD-like phenotypes while concurrently diminishing sexually dimorphic traits at multiple mechanistic levels. Transcriptomic analyses reveal that these effects are both developmentally and regionally specific, implicating critical biological processes related to synaptic function, mitochondrial activity, and splicing regulation in mediating these complex phenotypic outcomes.

METHODS

Animals

The generation of the *Chd8*-mutant mice with the Asn2373LysfsX2 mutation in the genetic background of C57BL/6J were described in a previous report [19]. These mice were back-crossed into the 129S1/SvImJ strain by mating heterozygous B6J mice with wild-type 129S1/SvImJ strain for at least five generations. The mice used in all experiments were F1 siblings produced by mating C57BL/6J HT and 129/Sv HT mice, which were maintained independently, with the parental sex of each inbred line counterbalanced. All mice were maintained and handled according to the Requirements of Animal Research at KAIST. The animals were housed under a 13:00–01:00 dark/light cycle environment.

PCR genotyping

For genotyping, the following primers were used. For1: CTT TAC CGG TGA GTT ACA TCA TCA, Rev1: CAG GCA AGC ACC TGG TGC ACA. To quantify mRNA levels, total brain RNAs were extracted from three pairs of WT and *Chd8*^{+/N2373K} male and female mice (P0), and cDNAs were synthesized using the TOPscript cDNA Synthesis Kit (Enzynomics, EZ005). SsoAdvanced SYBR Green Supremix (BIORAD, 1725260) and CFX96 Real-Time System were used for real-time PCR. The following primers were used. For2: GCG GAG CTG GAG ATG TGG TTA CAG, Rev2: TCT AGA GTT CGC TGG CTG TAC TGG T for CHD8. GAPDH: TCA GCA ATG CAT CCT GCA CCA CC, GAPDH: TGG CAG TGA TGG CAT GGA CTG TG for GAPDH and normalization. For sequencing validation of the knock-in (KI) mutation, PCR and gel extraction were performed on genomic DNA using the For1 and Rev1 primers.

Immunoblot analysis

After immunoblotting, HRP-conjugated secondary antibody signals for *Chd8* were detected by film exposure, while fluorescent secondary antibody signals were detected using the Odyssey Fc Dual Mode Imaging System. Signals were quantified using Image Studio Lite (Ver 4.0). The following antibodies were purchased: n-CHD8 (Bethyl, A301-224A), c-CHD8 (Bethyl, A301-225A), and β -actin (Sigma, A5316).

Behavioral tests

For nocturnal mice, all behavioral tests were conducted during the night (light-off periods) using age- and sex-matched mice. A minimum rest period of 2 days was provided between tests to ensure recovery and reduce stress. All animals were randomly assigned to test days and order, counterbalanced across genotype and sex to minimize potential bias. We did not control for estrous cycle variability, as the cycles of group-housed females are generally synchronized.

LABORAS

Each mouse was placed in an individual cage, and behaviors were recorded for 72 h, starting with the night cycle. Basal activities were recorded and automatically analyzed using the Laboratory Animal Behavior Observation Registration and Analysis System (LABORAS, Metris). Data from the 36-hour dark period were quantified and presented.

Open-field test

An empty white acrylic box measuring 40 × 40 × 40 cm, referred to as an open-field box, was used to monitor mouse activity under 100 lux illumination. Mice were placed in the box for 60 min, and their activity was recorded. The videos were analyzed using the EthoVision XT program. The “distance moved” by the mice was used as a measure of their activity level, while the “time spent in the center” of the box was used to assess anxiety-like behavior.

Repetitive behavior

Mice were individually placed in a home cage, a familiar environment, under 60 lux illumination. After a 10-minute habituation period, mouse activity was recorded for an additional 10 min. Self-grooming and digging behaviors were manually quantified during this recording period. For precise measurement of each behavior, two cameras were used to record from different angles.

Light-dark box test

The light-dark box consisted of two connected chambers: a white, open-roof chamber (21 × 29 × 20 cm) and a closed black chamber (21 × 13 × 20 cm), with a small entrance allowing movement between the two. The light chamber was illuminated at 600 lux. Mice could freely move between the light and dark chambers, typically seeking the dark chamber when anxious in the bright environment. The time spent in the light chamber was measured as an indicator of anxiety-related behavior.

Elevated plus-maze

The elevated plus-maze consists of two open arms and two closed arms, each measuring 5 × 30 cm. The closed arms have 30-cm-high walls, and the entire maze is elevated 50 cm above the floor. Mice were placed in the center of the maze and their movements were recorded for 8 min under 180 lux illumination. The time spent in each set of arms (open versus closed) was measured using the EthoVision XT program to assess anxiety-related behavior.

Three-chamber test

Mice were first habituated in the center chamber for 10 min, followed by 10 min of exploration in all three chambers (Session 1). After Session 1, an age- and sex-matched Social 1 mouse (C57BL/6J) was placed in a small container in the corner of one side chamber, while an object was placed in a container in the opposite side chamber. The mouse's movements were then recorded for 10 min (Session 2). In Session 3, the object was replaced with another age- and sex-matched Social 2 mouse (C57BL/6J), and the movements were recorded for another 10 min. Time spent in each chamber was analyzed using EthoVision XT 10.1, and sniffing time was manually quantified.

Direct social-interaction test

For two consecutive days before the test, each mouse was habituated to an acrylic direct social interaction box for 10 min. On the test day, each mouse was placed in the box with a sex-matched wild-type (WT, C57BL/6J) mouse, and their interactions were recorded for 10 min. The subject mouse's behaviors, such as nose-to-nose sniffing, body contact, and nose-to-body sniffing, were manually quantified.

Courtship ultrasonic vocalization (USV)

Ultrasonic vocalizations (USVs) were recorded using Avisoft Recorder software. An ultrasound microphone (Avisoft) was positioned 20 cm above the testing arena. Each mouse was placed in a home cage and habituated to the testing chamber for 5 min. Following habituation, an unfamiliar age-matched wild-type (WT, C57BL/6J) female mouse was introduced, and the USVs were recorded for 5 min. The recorded USV calls were then transferred to Avisoft SASlab Pro for analysis.

MRI: acquisitions

Five mice per group were used for the MRI studies (WTM, 36.2 ± 5.0 g; WTF, 26.5 ± 2.2 g; HTM 34.4 ± 3.4 g; HTF, 28.1 ± 2.6 g; HMM, 33.3 ± 1.9 g; and HMF, 25.9 ± 1.9 g). All MRI experiments were conducted on a Bruker Biospec 9.4 T/30-cm horizontal bore instrument with a 12.0-cm actively shielded insert, operating at a maximum gradient strength of 66 Gauss/cm and a rise time of 141 μ s. The mouse brain was positioned near the isocenter of the magnet, using an 86 mm inner diameter quadrature birdcage coil for excitation and a 10-mm receiver surface coil on the mouse's head. Magnetic field homogeneity was globally shimmed, followed by local optimization using the MAPSHIM protocol, targeting an ellipsoid volume covering the cerebrum (ParaVision 6.0.1, Bruker BioSpin). Single-shot GE-EPI sequences were acquired for total-vasculature perfusion mapping with parameters: TR/TE = 1000/11.6 ms, flip angle = 50°, receiver bandwidth = 300 kHz, spatial resolution = 156 μ m \times 156 μ m \times 500 μ m, 20 interleaved slices, slice thickness = 500 μ m, and 10 dummy scans. Physiological data, including heart rate, peripheral oxygen saturation, respiration, and end-tidal CO₂, were continuously monitored using a multiparameter physiological monitoring system, with temperature maintained at $37^\circ \pm 0.5^\circ$ C using a warm water blanket.

MRI: anesthetic regimes

Mice were initially anesthetized with 5% isoflurane (ISO) in a 1:4 mixture of oxygen and air for 3 to 4 min. The ISO concentration was then reduced to 2.5% for the MRI setup, and subsequently adjusted and maintained at 1.5% for the duration of the procedure. Data acquisition began 15 to 20 min after adjusting the ISO dose to ensure the anesthesia had stabilized. All experiments were completed within 1 h from the start of the first acquisition in each mouse. To ensure comparable depths of anesthesia across experimental groups, we measured baseline respiratory rates during imaging sessions. Baseline respiratory rates (mean \pm SD) were as follows: WTM, 142.1 ± 20.4 BPM; WTF, 143.7 ± 15.9 BPM; HTM, 136.6 ± 8.0 BPM; HTF, 148.3 ± 16.5 BPM; HMM, 139.5 ± 3.9 BPM; and HMF, 144.2 ± 10.1 BPM. Respiratory rates were similar across groups, except for HTM.

MRI: setup and stimulus designs

Two inhaled gas mixtures were utilized: one for control medical gas with anesthetics and the other for the hypoxic stimulus [53, 90]. These gases were connected to a breathing cone, with a transistor-transistor logic (TTL) signal synchronized with the MRI scanner to accurately switch between the two gases. A solenoid two-way pinch valve controlled the flow of medical gas to the animal, ensuring consistent gas pressure during experiments, while a three-channel programmable gas mixer (GSM-3 Gas Mixer, CWE Inc., Ardmore, PA) regulated the hypoxic gas stimulus. To efficiently remove exhaled and residual gas from the nose cone, a slightly negative pressure was maintained in the exhaust gas line. The normoxic baseline was set to 40% O₂ balanced with N₂ to ensure adequate oxygenation during anesthesia. The transient hypoxic stimulus, delivered without any inhaled anesthetics, used 100% N₂. Each run, lasting 3 min and 20 s, consisted of 20 s of normoxia followed by a cycle of 5 s of hypoxia and 5 s of normoxia, repeated three times. For each anesthetic condition in each animal, five runs (totaling 15 trials of 5-second hypoxia) were conducted to gather data for total vasculature-sensitive GE-EPI. To ensure adequate BOLD sensitivity, we calculated the voxel-wise temporal SNR as the mean signal divided by the SD of the baseline. The whole-brain temporal SNR values (mean \pm SD) were as follows: WTM, 23.3 ± 1.3 ; WTF, 24.3 ± 0.6 ; HTM, 23.9 ± 1.4 ; HTF, 23.2 ± 0.8 ; HMM, 23.8 ± 0.5 ; and HMF, 24.7 ± 0.6 . No significant group differences were detected by ANOVA.

MRI: Perfusion image analysis

All BOLD time series data for each mouse were analyzed using several tools and software packages, including the Analysis of Functional Neuroimages (AFNI) package [91], FMRIB Software Library (FSL), Advanced Normalization Tools (ANTs) [92], and custom MATLAB scripts (MathWorks). The preprocessing of individual EPI images involved the following steps: slice timing correction, image realignment, and linear detrending to remove signal drift.

Since anesthesia was used, head motion was expected to be minimal. Nonetheless, to ensure high stability in data collection, motion was quantified using frame-wise displacement across all EPI scans. The frame-wise displacements (mean \pm SD) were as follows: WTM, 9.8 ± 4.5 μ m; WTF, 8.3 ± 4.7 μ m; HTM, 8.5 ± 3.4 μ m; HTF, 8.1 ± 3.2 μ m; HMM, 8.4 ± 3.8 μ m; and HMF, 7.6 ± 2.8 μ m. As expected under anesthesia, head motion was minimal, and no significant group differences were observed.

Cerebral blood volume (CBV) and cerebral blood flow (CBF) were quantified during the perfusion analysis, and group-averaged perfusion maps were generated within the mouse brain template space through a series of steps. First, T2-weighted anatomical images (78 μ m \times 78 μ m \times 500 μ m) from all individual subjects were averaged using linear transformations to create a mouse brain template (anatomy template). Next, the Allen Mouse Brain Atlas and its labels were normalized to this mouse brain template using nonlinear transformations (Allen's Atlas \rightarrow anatomy template). Third, perfusion maps from individual EPI datasets (156 μ m \times 156 μ m \times 500 μ m) were co-registered to the anatomy template using linear transformations (perfusion map \rightarrow anatomy template). Finally, the perfusion maps aligned to the anatomy template were statistically analyzed based on the Allen's Atlas space, integrating the steps (perfusion map \rightarrow anatomy template \leftarrow Allen's Atlas) [93].

The perfusion metrics were quantified using the dynamic susceptibility contrast (DSC) tracer kinetic theory [94–96], following the methods outlined in previous studies [53, 90]. Briefly, the EPI signal intensity change in each voxel was converted to the relaxation rate change $\Delta R2^*$ using the formula for hypoxia-induced relative change: $e^{-TE \cdot \Delta R2^*}$. The venous output function (VOF) and arterial input function (AIF) for the perfusion analysis were determined by calculating the area under the curve (AUC) within the first 12 s after stimulus onset and the peak intensity of the $\Delta R2^*(t)$ signal [90], utilizing a vascular-atlas-based mask for VOF and AIF [97]. Subsequently, CBV was calculated as the ratio of the voxel's AUC to the AUC of the AIF, corrected by the VOF. The tissue concentration response (Ct(t)), proportional to CBF, was defined as the convolution of the tissue response function R(t) [CBF \times residue function R(t)] and the AIF, given by $Ct(t) = CBF \cdot AIF \otimes R(t)$ [98]. The tissue impulse response function was obtained through deconvolution using the singular value decomposition (SVD) approach with a fixed threshold (20% cutoff) [53]. CBF was then determined as the maximum height of the tissue impulse response function.

In our whole-brain perfusion experiments using 20 slices at 0.5-mm thickness, the most anterior regions (e.g., olfactory bulb, frontal pole) and the most posterior regions (e.g., medulla and cerebellum) were only partially included. In addition, the ventral regions (olfactory ventral, retrohippocampal area, cortical subplate, etc.) exhibited distortion and signal loss in the EPI images. Therefore, these regions were excluded from the quantitative analyses shown in Fig. 3b and Fig. 4b.

To assess whether the measured CBV was influenced by total brain volume, we quantified intracranial volume covered by MRI (mean \pm SD): WTM, 39.8 ± 0.6 mm³; WTF, 40.3 ± 0.9 mm³; HTM, 40.5 ± 1.2 mm³; HTF, 41.1 ± 0.6 mm³; HMM, 41.9 ± 0.8 mm³; and HMF, 42.1 ± 0.7 mm³. We then performed ANCOVA with brain volume and body weight as covariates and compared the results with those obtained from ANOVA (Supplementary Fig. 3e).

Neuropixels: surgery, recordings, and analyses

A total of 52 mice were used for Neuropixels 1.0 recordings under urethane anesthesia (male WT: 9, male HT: 9, male HM: 9; female WT: 7, female HT: 7, female HM: 9; postnatal 9–16 weeks). An additional 12 mice were used for head-fixed awake Neuropixels 1.0 recordings (male WT: 3, male HM: 3; female WT: 3, female HM: 3; postnatal 9–16 weeks) to assess whether anesthetic state qualitatively altered genotype- and sex-dependent effects. For anesthetized *in vivo* recordings, mice were secured in a stereotaxic frame under urethane anesthesia (1.5 g/kg, *i.p.*). Body temperature was continuously monitored and maintained with a TC-1000 temperature controller (CWE), and the eyes were coated with Vaseline to prevent corneal drying. To minimize state-related variability, all animals received the same weight-adjusted urethane dose, recordings were initiated after a fixed post-induction interval, and recording durations were matched across animals. Respiratory rate and reflexes remained stable throughout, and a pinch-response test was performed at the start of each session to confirm a stable anesthetic depth. No supplemental doses were required, consistent with the use of urethane as a highly stable and reproducible anesthetic for long-duration recordings. For head-fixed awake recordings, mice underwent a craniotomy one week prior to the experiment. A custom head-plate was affixed to the skull using dental acrylic and titanium screws to ensure stable head fixation. A ground/reference screw was implanted over the nasal bone. Animals were habituated to the head-fixation apparatus for at least three days. On the recording day, mice were secured in the head-post clamp, and data were collected in a rig equipped with noise shielding and vibration isolation.

Neuronal activity was recorded across various brain regions, including cortical and thalamic areas. Two Neuropixels 1.0 probes were inserted

bilaterally at coordinates AP 2.1 mm, ML \pm 1.6 mm from bregma, and -4.5 mm from the brain surface. The probes were coated with the fluorescent dye Dil (D7757, Thermo Fisher Scientific) to localize the recording sites. The location of each probe channel was determined by examining post-processed brain tissue for each mouse using Allen-CCF (<https://github.com/cortex-lab/allenCCF>). Recordings used for analysis were conducted for 45 min following an hour of post-insertion stabilization. Simultaneous recordings were made from 384 sites on a single Neuropixels probe. Electrophysiology data were acquired using Open-Ephys (<https://open-ephys.org/gui>). To obtain single-unit data, electrode signals were filtered between 300 Hz and 6000 Hz and sampled at 30,000 Hz. Spike sorting was performed using Kilosort1.5 (<https://github.com/MouseLand/Kilosort/>) [99], followed by manual curation to select isolated single units using Phy (<https://github.com/cortex-lab/phy>). Single units were selected after comprehensive inspection based on traditional measures such as inter-spike intervals (ISIs), autocorrelation, and waveform shape. The single-unit data were then analyzed to calculate firing rates using custom MATLAB code (www.mathworks.com).

Local field potential (LFP) data (sampling rate: 2000 Hz) were band-pass filtered between 0.1 and 200 Hz using a 3rd-order Butterworth filter, and a notch filter was applied to attenuate power line noise. The filtered LFP signals were analyzed using custom MATLAB scripts (www.mathworks.com). Fourier transformation was used to compute the power spectrum for each electrode channel. This was achieved by segmenting the data into 30-second bins and applying the Fast Fourier Transform (FFT) within each bin. The power spectra were then normalized by dividing the power at each frequency by the total power across all frequencies. The frequency bands of interest were defined as delta (0.1–4 Hz), theta (4–12 Hz), beta (13–30 Hz), low gamma (31–55 Hz), and high gamma (65–130 Hz). For each electrode channel, the power within these frequency bands was calculated by summing the normalized power spectra within the defined band limits. The power values for each frequency band and brain region were then log-transformed to facilitate analysis. Fold changes were calculated by first averaging the log-transformed power values for each group, and then dividing the group average by the average of either the male WT or the female WT group. This approach allowed for the comparison of relative changes in power across different frequency bands and between experimental groups. At the end of the experiment, brains were extracted, then sectioned (70 μ m slices). The probe tracks were mapped onto brain atlas coordinates to verify targeting accuracy and recording depth using SHARP-Track ss (<https://doi.org/10.1101/447995>). High-resolution coronal sections were registered to the Allen Mouse Brain Atlas, and the Neuropixels shank was manually aligned to the reconstructed track to determine the entry point, insertion angle, and depth profile. Each electrode site and each sorted unit was assigned an anatomical depth and brain region based on this reconstruction, and only units and LFP channels located within brain regions that were consistently sampled across all animals were included in between-group comparisons, ensuring that genotype- or sex-dependent differences could not be attributed to differential laminar or regional sampling.

Electrophysiology

For adult hippocampus recording, acute sagittal brain slices were obtained by anesthetizing P56 mice with isoflurane and extracting the brain after perfusion with NMDG buffer (pH 7.3–7.4 and 300–310 mOsm/kg) containing NMDG (100 mM), N-acetylcysteine (NAC, 12 mM), NaHCO₃ (30 mM), HEPES (20 mM), Glucose (25 mM), Thiourea (2 mM), Na-Ascorbate (5 mM), Na-pyruvate (3 mM), KCl (2.5 mM), NaH₂PO₄ (1.25 mM), CaCl₂ (0.5 mM), and MgSO₄ (10 mM). The extracted brains were sliced by vibratome (VT1200s, Leica) with 300 μ m thickness and were incubated in 32 °C recovery chamber for 11 min and then transferred to RT with HEPES aCSF for 1 h, which consists of NaCl (92 mM), NAC (12 mM), NaHCO₃ (30 mM), HEPES (20 mM), glucose (25 mM), thiourea (2 mM), Na-ascorbate (5 mM), Na-pyruvate (3 mM), KCl (2.5 mM), NaH₂PO₄ (1.25 mM), MgCl₂ (1.3 mM), and CaCl₂ (2.5 mM).

The whole-cell voltage clamp was conducted under circulation of aCSF consist of NaCl (125 mM), NaHCO₃ (25 mM), KCl (2.5 mM), NaH₂PO₄ (1.25 mM), D-glucose (10 mM), MgCl₂ (1.3 mM), and CaCl₂ (2.5 mM). Thin-walled borosilicate capillaries (30-0065, Harvard Apparatus) were used to make pipettes with resistance 2.3–3.5 M Ω via a two-step vertical puller (PC-10, Narishige). For sEPSC and mEPSC recordings, pipettes were filled with an internal solution composed of, in mM: 117 CsMeSO₄, 10 EGTA, 8 NaCl, 10 TEACl, 10 HEPES, 4 Mg-ATP, 0.3 Na-GTP, 5 QX-314. For sIPSC and mIPSC recordings, the internal solution contained, in mM: 115 CsCl, 10 EGTA, 8 NaCl, 10 TEACl, 10 HEPES, 4 Mg-ATP, 0.3 Na-GTP, 5 QX-314. All

internal solutions were titrated to pH 7.35 and adjusted to an osmolarity of 285 mOsm. For sEPSC experiments, 60 μ M picrotoxin (Sigma) was added to the aCSF. For mEPSC experiments, 60 μ M picrotoxin and 0.5 μ M tetrodotoxin (Tocris) were added. For sIPSC experiments, 10 μ M NBQX (Tocris), 50 μ M D-AP5 (Tocris) were added. For mIPSC experiments 10 μ M NBQX (Tocris), 50 μ M D-AP5 (Tocris), 0.5 μ M tetrodotoxin (Tocris) were added. For cell property experiments, 10 μ M NBQX (Tocris), 50 μ M D-AP5 (Tocris), and 60 μ M picrotoxin.

We used only the neurons in specific property ranges (access resistance/Ra < 20 M Ω , membrane resistance/Rm > 100 M Ω , cell capacitance/Cm > 100 pF) for recordings and analyses. The neurons within these ranges did not display genotype/sex differences. Signals were filtered at 2 kHz and digitized at 10 kHz using the Multiclamp 700B Amplifier (Molecular Devices) and the Digidata 1550 Digitizer (Molecular Devices). Cells were approached with an internal solution-filled pipette to establish a giga seal, followed by gentle suction to rupture the membrane and establish whole-cell configuration, with cells maintained at -70 mV. After stabilizing the voltage-clamped cells (\sim 3 min post-rupture), recordings were obtained. Access resistance was continuously monitored throughout the stabilization period and immediately before and after data acquisition. The acquired data were analyzed using Clampfit 10 software (Molecular Devices).

RNA-Seq analyses

Whole brains from P0, P25, and P56 mice, along with dissected prefrontal cortex, striatum, and hippocampus from P56 mice, were preserved in RNAlater solution (Ambion) to stabilize RNA. RNA extraction, library preparation, cluster generation, and sequencing were performed by Macrogen. Sequencing was conducted on an Illumina HiSeq 4000 platform, achieving an average read depth of 70–90 million paired-end reads (2 \times 101 bp). Image analysis and base calling were performed using Illumina Real-Time Analysis (RTA) software, and raw BCL files were converted to FASTQ format using the Illumina bcl2fastq package.

The dataset comprised 180 samples across two experimental designs. For developmental analysis, 90 whole-brain samples were collected from P0, P25, and P56 mice, spanning both sexes and three genotypes (wild-type, heterozygous, homozygous). Sequencing for each age group was conducted in a separate batch (30 samples per batch), resulting in complete confounding between age and batch. For tissue-specific analysis at P56, 90 additional samples were collected from the prefrontal cortex, hippocampus, and striatum, again including both sexes and genotypes. Each tissue type was sequenced in its own batch, introducing confounding between tissue and batch. To account for batch confounding, differential gene expression (DGE) analyses were performed independently within each group (i.e., per age or per tissue type) using the DESeq2 package. Within each group, genotype and sex were modeled as factors, and appropriate covariates were included where applicable.

Transcript abundance was quantified using Salmon (v1.1.0) in quasi-mapping mode with GC bias correction, aligning to the *Mus musculus* reference transcriptome (GRCm38). Gene-level abundance estimates were imported into R (v3.5.3) using the tximport package. DGE analysis was conducted using DESeq2 (v1.30.1), which normalizes read counts by estimating size factors and models the data with a negative binomial distribution. Significance was determined using the Benjamini–Hochberg procedure to correct for multiple testing, with genes considered differentially expressed at adjusted $p < 0.05$.

Gene Ontology (GO) enrichment analysis was performed using DAVID (v6.8). Mouse gene symbols were converted to human orthologs using the Mouse Genome Informatics (MGI) database. Additionally, Gene Set Enrichment Analysis (GSEA) was carried out with the GSEAPreranked module from the GSEA software (MSigDB v7.5.1). Ranked gene lists comparing wild-type and *Chd8* heterozygous mice were tested against predefined gene sets using 1,000 permutations and a classic enrichment score. Gene sets with a false discovery rate (FDR) < 0.05 were considered significantly enriched.

Statistical analysis

All behavioral datasets were analyzed using two-way ANOVA with genotype and sex as fixed factors. Primary endpoints were pre-specified as: (1) locomotor activity (distance in LABORAS and open field), (2) anxiety-like behavior (open-field center time, light–dark light-chamber time, EPM closed-arm time), (3) self-grooming (LABORAS and home-cage assays), and (4) social behavior (three-chamber preference indices and direct-interaction time); secondary measures (e.g., sniffing times, USV parameters) were not included in multiplicity correction. When the genotype \times sex

interaction was significant ($p < 0.05$), we performed pre-planned simple-effects tests between genotypes within each sex and adjusted p values using the Holm-Sidak step-down procedure (FWER = 0.05 within each primary endpoint); when no interaction but a genotype main effect was present, we used one-way ANOVA or t tests within sex. Supplementary Table 1 summarizes, for each endpoint and sex, group means, standard deviations, 95% confidence intervals, absolute mean differences (HT–WT and HM–WT), and Cohen's d for WT–HT and WT–HM contrasts; per-sex sample sizes are given there and in all figure legends. Outliers were identified using Grubbs' test ($\alpha = 0.05$) and removed only when statistically justified, and all analyses were performed in GraphPad Prism.

DATA AVAILABILITY

The RNA-Seq datasets available under GEO accession numbers GSE275918 and GSE275742 provide gene expression data from the whole brain at developmental stages P0, P25, and P56, and from specific brain regions (cortex, hippocampus, and striatum) at P56, respectively. These datasets are also combined under the SuperSeries GSE275960.

REFERENCES

- Barnard RA, Pomaville MB, O'Roak BJ. Mutations and modeling of the chromatin remodeler CHD8 define an emerging autism etiology. *Front Neurosci.* 2015;9:477.
- Hoffmann A, Spengler A. Chromatin remodeler CHD8 in autism and brain development. *J Clin Med.* 2021;10:366.
- Merner N, Forgeot d'Arc B, Bell SC, Maussion G, Peng H, Gauthier J, et al. A de novo frameshift mutation in chromodomain helicase DNA-binding domain 8 (CHD8): A case report and literature review. *Am J Med Genet A.* 2016;170A:1225–35.
- Bernier R, Golzio C, Xiong B, Stessman HA, Coe BP, Penn O, et al. Disruptive CHD8 mutations define a subtype of autism early in development. *Cell.* 2014;158:263–76.
- Beighley JS, Hudac CM, Arnett AB, Peterson JL, Gerdtz J, Wallace AS, et al. Clinical phenotypes of carriers of mutations in CHD8 or its conserved target genes. *Biol Psychiatry.* 2020;87:123–31.
- An Y, Zhang L, Liu W, Jiang Y, Chen X, Lan X, et al. De novo variants in the Helicase-C domain of CHD8 are associated with severe phenotypes including autism, language disability and overgrowth. *Hum Genet.* 2020;139:499–512.
- Dingemans AJM, Truijien KMG, van de Ven S, Bernier R, Bongers E, Bouman A, et al. The phenotypic spectrum and genotype-phenotype correlations in 106 patients with variants in major autism gene CHD8. *Transl Psychiatry.* 2022;12:421.
- Sorrentino U, Boesch S, Doummar D, Ravelli C, Serranova T, Indelicato E, et al. CHD8-related disorders redefined: an expanding spectrum of dystonic phenotypes. *J Neurol.* 2024;271:2859–65.
- Mitchel MW, Myers SM, Heidlebaugh AR, Taylor CM, Rea H, Neuhaus E et al. CHD8-Related Neurodevelopmental Disorder with Overgrowth. In: Adam MP, Feldman J, Mirzaa GM, Pagon RA, Wallace SE, Amemiya A (eds). *Seattle (WA): GeneReviews((R))*, 1993.
- Basson MA. Neurodevelopmental functions of CHD8: new insights and questions. *Biochem Soc Trans.* 2024;52:15–27.
- Katayama Y, Nishiyama M, Shoji H, Ohkawa Y, Kawamura A, Sato T, et al. CHD8 haploinsufficiency results in autistic-like phenotypes in mice. *Nature.* 2016;537:675–9.
- Platt RJ, Zhou Y, Slaymaker IM, Shetty AS, Weisbach NR, Kim JA, et al. Chd8 mutation leads to autistic-like behaviors and impaired striatal circuits. *Cell Rep.* 2017;19:335–50.
- Gompers AL, Su-Feher L, Ellegood J, Copping NA, Riyadh MA, Stradleigh TW, et al. Germine Chd8 haploinsufficiency alters brain development in mouse. *Nat Neurosci.* 2017;20:1062–73.
- Xu Q, Liu YY, Wang X, Tan GH, Li HP, Hulbert SW, et al. Autism-associated CHD8 deficiency impairs axon development and migration of cortical neurons. *Mol Autism.* 2018;9:65.
- Breuss MW, Gleeson JG. When size matters: CHD8 in autism. *Nat Neurosci.* 2016;19:1430–2.
- Durak O, Gao F, Kaeser-Woo YJ, Rueda R, Martorell AJ, Nott A, et al. Chd8 mediates cortical neurogenesis via transcriptional regulation of cell cycle and Wnt signaling. *Nat Neurosci.* 2016;19:1477–88.
- Suetterlin P, Hurlley S, Mohan C, Riegman KLH, Pagani M, Caruso A, et al. Altered neocortical gene expression, brain overgrowth and functional over-connectivity in Chd8 haploinsufficient mice. *Cereb Cortex.* 2018;28:2192–206.
- Andreae LC, Basson MA. Sex bias in autism: new insights from Chd8 mutant mice? *Nat Neurosci.* 2018;21:1144–6.
- Jung H, Park H, Choi Y, Kang H, Lee E, Kweon H, et al. Sexually dimorphic behavior, neuronal activity, and gene expression in Chd8-mutant mice. *Nat Neurosci.* 2018;21:1218–28.
- Jimenez JA, Ptacek TS, Tuttle AH, Schmid RS, Moy SS, Simon JM, et al. Chd8 haploinsufficiency impairs early brain development and protein homeostasis later in life. *Mol Autism.* 2020;11:74.
- Hulbert SW, Wang X, Gbadegesin SO, Xu Q, Xu X, Jiang YH. A novel Chd8 mutant mouse displays altered ultrasonic vocalizations and enhanced motor coordination. *Autism Res.* 2020;13:1685–97.
- Cotney J, Muhle RA, Sanders SJ, Liu L, Willsey AJ, Niu W, et al. The autism-associated chromatin modifier CHD8 regulates other autism risk genes during human neurodevelopment. *Nat Commun.* 2015;6:6404.
- Sugathan A, Biagioli M, Golzio C, Erdin S, Blumenthal I, Manavalan P, et al. CHD8 regulates neurodevelopmental pathways associated with autism spectrum disorder in neural progenitors. *Proc Natl Acad Sci USA.* 2014;111:E4468–4477.
- Wang P, Lin M, Pedrosa E, Hrabovsky A, Zhang Z, Guo W, et al. CRISPR/Cas9-mediated heterozygous knockout of the autism gene CHD8 and characterization of its transcriptional networks in neurodevelopment. *Mol Autism.* 2015;6:55.
- Zhao C, Dong C, Frah M, Deng Y, Marie C, Zhang F, et al. Dual requirement of CHD8 for chromatin landscape establishment and histone methyltransferase recruitment to promote CNS myelination and repair. *Dev Cell.* 2018;45:753–68 e758.
- Wade AA, Lim K, Catta-Preta R, Nord AS. Common CHD8 genomic targets contrast with model-specific transcriptional impacts of CHD8 haploinsufficiency. *Front Mol Neurosci.* 2018;11:481.
- Sood S, Weber CM, Hodges HC, Krokhotin A, Shalizi A, Crabtree GR. CHD8 dosage regulates transcription in pluripotency and early murine neural differentiation. *Proc Natl Acad Sci USA.* 2020;117:22331–40.
- Ellingford RA, Panasiuk MJ, de Meritens ER, Shaunak R, Naybour L, Browne L, et al. Cell-type-specific synaptic imbalance and disrupted homeostatic plasticity in cortical circuits of ASD-associated Chd8 haploinsufficient mice. *Mol Psychiatry.* 2021;26:3614–24.
- Kweon H, Jung WB, Im GH, Ryoo J, Lee JH, Do H, et al. Excitatory neuronal CHD8 in the regulation of neocortical development and sensory-motor behaviors. *Cell Rep.* 2021;34:108780.
- Kawamura A, Katayama Y, Kakegawa W, Ino D, Nishiyama M, Yuzaki M, et al. The autism-associated protein CHD8 is required for cerebellar development and motor function. *Cell Rep.* 2021;35:108932.
- Hurlley S, Mohan C, Suetterlin P, Ellingford R, Riegman KLH, Ellegood J, et al. Distinct, dosage-sensitive requirements for the autism-associated factor CHD8 during cortical development. *Mol Autism.* 2021;12:16.
- Tabbaa M, Knoll A, Levitt P. Mouse population genetics phenocopies heterogeneity of human Chd8 haploinsufficiency. *Neuron.* 2023;111:539–56 e535.
- Nita A, Muto Y, Katayama Y, Matsumoto A, Nishiyama M, Nakayama KI. The autism-related protein CHD8 contributes to the stemness and differentiation of mouse hematopoietic stem cells. *Cell Rep.* 2021;34:108688.
- Cherepanov SM, Gerasimenko M, Yuhi T, Furuhashi K, Tsuji C, Yokoyama S, et al. Oxytocin ameliorates impaired social behavior in a Chd8 haploinsufficiency mouse model of autism. *BMC Neurosci.* 2021;22:32.
- Ellingford RA, Tojo M, Basson MA, Andreae LC. Male-Dominant effects of Chd8 haploinsufficiency on synaptic phenotypes during development in mouse pre-frontal cortex. *ACS Chem Neurosci.* 2024;15:1635–42.
- Kawamura A, Katayama Y, Nishiyama M, Shoji H, Tokuoaka K, Ueta Y, et al. Oligodendrocyte dysfunction due to Chd8 mutation gives rise to behavioral deficits in mice. *Hum Mol Genet.* 2020;29:1274–91.
- Jimenez JA, Simon JM, Hu W, Moy SS, Harper KM, Liu CW, et al. Developmental pyrethroid exposure and age influence phenotypes in a Chd8 haploinsufficient autism mouse model. *Sci Rep.* 2022;12:5555.
- Astorkia M, Liu Y, Pedrosa EM, Lachman HM, Zheng D. Molecular and network disruptions in neurodevelopment uncovered by single cell transcriptomics analysis of CHD8 heterozygous cerebral organoids. *Heliyon.* 2024;10:e34862.
- Lee SY, Kweon H, Kang H, Kim E. Age-differential sexual dimorphism in CHD8-S62X-mutant mouse behaviors. *Front Mol Neurosci.* 2022;15:1022306.
- Lee SY, Kweon H, Kang H, Kim E. Age-differential sexual dimorphisms in CHD8-S62X-mutant mouse synapses and transcriptomes. *Front Mol Neurosci.* 2023;16:111388.
- Megagiannis P, Mei Y, Yan RE, Yuan L, Wilde JJ, Eckersberg H, et al. Autism-associated CHD8 controls reactive gliosis and neuroinflammation via remodeling chromatin in astrocytes. *Cell Rep.* 2024;43:114637.
- Shi X, Lu C, Corman A, Nikish A, Zhou Y, Platt RJ, et al. Heterozygous deletion of the autism-associated gene CHD8 impairs synaptic function through widespread changes in gene expression and chromatin compaction. *Am J Hum Genet.* 2023;110:1750–68.
- Kawamura A, Nishiyama M. Deletion of the autism-related gene Chd8 alters activity-dependent transcriptional responses in mouse postmitotic neurons. *Commun Biol.* 2023;6:593.
- Li B, Zhao H, Tu Z, Yang W, Han R, Wang L, et al. CHD8 mutations increase gliogenesis to enlarge brain size in the nonhuman primate. *Cell Discov.* 2023;9:27.

45. Yu Y, Zhang B, Ji P, Zuo Z, Huang Y, Wang N, et al. Changes to gut amino acid transporters and microbiome associated with increased E/I ratio in Chd8(+/-) mouse model of ASD-like behavior. *Nat Commun.* 2022;13:1151.
46. Shiraishi T, Katayama Y, Nishiyama M, Shoji H, Miyakawa T, Mizoo T, et al. The complex etiology of autism spectrum disorder due to missense mutations of CHD8. *Mol Psychiatry.* 2024;29:2145–60.
47. Nitahara K, Kawamura A, Kitamura Y, Kato K, Namekawa SH, Nishiyama M. Chromatin remodeler CHD8 is required for spermatogonial proliferation and early meiotic progression. *Nucleic Acids Res.* 2024;52:2995–3010.
48. Weissberg O, Elliott E. The mechanisms of CHD8 in neurodevelopment and autism spectrum disorders. *Genes (Basel).* 2021;12:1133.
49. O'Roak BJ, Vives L, Fu W, Egerton JD, Stanaway IB, Phelps IG, et al. Multiplex targeted sequencing identifies recurrently mutated genes in autism spectrum disorders. *Science.* 2012;338:1619–22.
50. Stessman HA, Xiong B, Coe BP, Wang T, Hoekzema K, Fenckova M, et al. Targeted sequencing identifies 91 neurodevelopmental-disorder risk genes with autism and developmental-disability biases. *Nat Genet.* 2017;49:515–26.
51. Threadgill DW, Dlugosz AA, Hansen LA, Tennenbaum T, Lichti U, Yee D, et al. Targeted disruption of mouse EGF receptor: effect of genetic background on mutant phenotype. *Science.* 1995;269:230–4.
52. Yasin H, Gibson WT, Langlois S, Stowe RM, Tsang ES, Lee L, et al. A distinct neurodevelopmental syndrome with intellectual disability, autism spectrum disorder, characteristic facies, and macrocephaly is caused by defects in CHD8. *J Hum Genet.* 2019;64:271–80.
53. Le TT, Im GH, Lee CH, Choi SH, Kim SG. Mapping cerebral perfusion in mice under various anesthesia levels using highly sensitive BOLD MRI with transient hypoxia. *Sci Adv.* 2024;10:eadm7605.
54. Steinmetz NA, Aydin C, Lebedeva A, Okun M, Pachitariu M, Bauza M, et al. Neuropixels 2.0: A miniaturized high-density probe for stable, long-term brain recordings. *Science.* 2021;372:eabf4588.
55. Hara K, Harris RA. The anesthetic mechanism of urethane: the effects on neurotransmitter-gated ion channels. *Anesth Analg.* 2002;94:313–8. table of contents
56. Maggi CA, Meli A. Suitability of urethane anesthesia for physiopharmacological investigations in various systems. Part 1: General considerations. *Experientia.* 1986;42:109–14.
57. Sorrenti V, Cecchetto C, Maschietto M, Fortinguerra S, Buriani A, Vassanelli S. Understanding the effects of anesthesia on cortical electrophysiological recordings: a scoping review. *Int J Mol Sci.* 2021;22:1286.
58. Speigel IA, Hemmings HC Jr. Relevance of cortical and hippocampal interneuron functional diversity to general anesthetic mechanisms: a narrative review. *Front Synaptic Neurosci.* 2021;13:812905.
59. Huh Y, Cho J. Urethane anesthesia depresses activities of thalamocortical neurons and alters its response to nociception in terms of dual firing modes. *Front Behav Neurosci.* 2013;7:141.
60. Haider B, Hausser M, Carandini M. Inhibition dominates sensory responses in the awake cortex. *Nature.* 2013;493:97–100.
61. Subramanian A, Tamayo P, Mootha VK, Mukherjee S, Ebert BL, Gillette MA, et al. Gene set enrichment analysis: a knowledge-based approach for interpreting genome-wide expression profiles. *Proc Natl Acad Sci USA.* 2005;102:15545–50.
62. Voineagu I, Wang X, Johnston P, Lowe JK, Tian Y, Horvath S, et al. Transcriptomic analysis of autistic brain reveals convergent molecular pathology. *Nature.* 2011;474:380–4.
63. Werling DM, Parikshak NN, Geschwind DH. Gene expression in human brain implicates sexually dimorphic pathways in autism spectrum disorders. *Nat Commun.* 2016;7:10717.
64. Abrahams BS, Arking DE, Campbell DB, Mefford HC, Morrow EM, Weiss LA, et al. SFARI Gene 2.0: a community-driven knowledgebase for the autism spectrum disorders (ASDs). *Mol Autism.* 2013;4:36.
65. Darnell JC, Van Driesche SJ, Zhang C, Hung KY, Mele A, Fraser CE, et al. FMRP stalls ribosomal translocation on mRNAs linked to synaptic function and autism. *Cell.* 2011;146:247–61.
66. Iossifov I, O'Roak BJ, Sanders SJ, Ronemus M, Krumm N, Levy D, et al. The contribution of de novo coding mutations to autism spectrum disorder. *Nature.* 2014;515:216–21.
67. Xu LM, Li JR, Huang Y, Zhao M, Tang X, Wei L. AutismKB: an evidence-based knowledgebase of autism genetics. *Nucleic Acids Res.* 2012;40:D1016–1022.
68. Yang C, Li J, Wu Q, Yang X, Huang AY, Zhang J, et al. AutismKB 2.0: a knowledgebase for the genetic evidence of autism spectrum disorder. *Database (Oxford).* 2018;2018:bay106.
69. Robinson EB, Lichtenstein P, Anckarsater H, Hapke F, Ronald A. Examining and interpreting the female protective effect against autistic behavior. *Proc Natl Acad Sci USA.* 2013;110:5258–62.
70. Gockley J, Willsey AJ, Dong S, Dougherty JD, Constantino JN, Sanders SJ. The female protective effect in autism spectrum disorder is not mediated by a single genetic locus. *Mol Autism.* 2015;6:25.
71. Dougherty JD, Marrus N, Maloney SE, Yip B, Sandin S, Turner TN, et al. Can the “female protective effect” liability threshold model explain sex differences in autism spectrum disorder? *Neuron.* 2022;110:3243–62.
72. Zhang Y, Li N, Li C, Zhang Z, Teng H, Wang Y, et al. Genetic evidence of gender difference in autism spectrum disorder supports the female-protective effect. *Transl Psychiatry.* 2020;10:4.
73. Lawrence KE, Hernandez LM, Fuster E, Padgaonkar NT, Patterson G, Jung J, et al. Impact of autism genetic risk on brain connectivity: a mechanism for the female protective effect. *Brain.* 2022;145:378–87.
74. Wigdor EM, Weiner DJ, Grove J, Fu JM, Thompson WK, Carey CE, et al. The female protective effect against autism spectrum disorder. *Cell Genom.* 2022;2:100134.
75. Werling DM, Geschwind DH. Sex differences in autism spectrum disorders. *Curr Opin Neurol.* 2013;26:146–53.
76. Werling DM, Geschwind DH. Recurrence rates provide evidence for sex-differential, familial genetic liability for autism spectrum disorders in multiplex families and twins. *Mol Autism.* 2015;6:27.
77. Werling DM, Lowe JK, Luo R, Cantor RM, Geschwind DH. Replication at chromosome 20p13 and identification of suggestive sex-differential risk loci for autism spectrum disorder. *Mol Autism.* 2014;5:13.
78. Werling DM, Geschwind DH. Understanding sex bias in autism spectrum disorder. *Proc Natl Acad Sci USA.* 2013;110:4868–9.
79. Ferri SL, Abel T, Brodtkin ES. Sex differences in autism spectrum disorder: a review. *Curr Psychiatry Rep.* 2018;20:9.
80. Hull L, Lai MC, Baron-Cohen S, Allison C, Smith P, Petrides KV, et al. Gender differences in self-reported camouflaging in autistic and non-autistic adults. *Autism.* 2020;24:352–63.
81. Kissel LT, Werling DM. Neural transcriptomic analysis of sex differences in autism spectrum disorder: current insights and future directions. *Biol Psychiatry.* 2022;91:53–60.
82. Hernandez LM, Lawrence KE, Padgaonkar NT, Inada M, Hoekstra JN, Lowe JK, et al. Imaging-genetics of sex differences in ASD: distinct effects of OXTR variants on brain connectivity. *Transl Psychiatry.* 2020;10:82.
83. Lai MC, Baron-Cohen S, Buxbaum JD. Understanding autism in the light of sex/gender. *Mol Autism.* 2015;6:24.
84. Napolitano A, Schiavi S, La Rosa P, Rossi-Espagnet MC, Pettillo S, Bottino F, et al. Sex differences in autism spectrum disorder: diagnostic, neurobiological, and behavioral features. *Front Psychiatry.* 2022;13:889636.
85. Martin J. Why are females less likely to be diagnosed with ADHD in childhood than males? *Lancet Psychiatry.* 2024;11:303–10.
86. May T, Adesina I, McGillivray J, Rinehart NJ. Sex differences in neurodevelopmental disorders. *Curr Opin Neurol.* 2019;32:622–6.
87. Hafner H. Gender differences in schizophrenia. *Psychoneuroendocrinology.* 2003;28:17–54.
88. Leung A, Chue P. Sex differences in schizophrenia, a review of the literature. *Acta Psychiatr Scand Suppl.* 2000;401:3–38.
89. Yim KM, Baumgartner M, Krenzer M, Rosales Larios MF, Hill-Terán G, Nottoli T, et al. Cell-type-specific dysregulation of gene expression due to Chd8 haploinsufficiency during mouse cortical development. *Cell Genomics.* 2025;5. <https://doi.org/10.1101/2024.08.14.608000>.
90. Lee D, Le TT, Im GH, Kim SG. Whole-brain perfusion mapping in mice by dynamic BOLD MRI with transient hypoxia. *J Cereb Blood Flow Metab.* 2022;42:2270–86.
91. Cox RW. AFNI: software for analysis and visualization of functional magnetic resonance neuroimages. *Comput Biomed Res.* 1996;29:162–73.
92. Avants BB, Tustison NJ, Song G, Cook PA, Klein A, Gee JC. A reproducible evaluation of ANTs similarity metric performance in brain image registration. *Neuroimage.* 2011;54:2033–44.
93. Jung WB, Shim HJ, Kim SG. Mouse BOLD fMRI at ultrahigh field detects somatosensory networks including thalamic nuclei. *Neuroimage.* 2019;195:203–14.
94. Villringer A, Rosen BR, Belliveau JW, Ackerman JL, Lauffer RB, Buxton RB, et al. Dynamic imaging with lanthanide chelates in normal brain: contrast due to magnetic susceptibility effects. *Magn Reson Med.* 1988;6:164–74.
95. Rosen BR, Belliveau JW, Vevea JM, Brady TJ. Perfusion imaging with NMR contrast agents. *Magn Reson Med.* 1990;14:249–65.
96. Ostergaard L, Weisskoff RM, Chesler DA, Gyldensted C, Rosen BR. High resolution measurement of cerebral blood flow using intravascular tracer bolus passages. Part I: Mathematical approach and statistical analysis. *Magn Reson Med.* 1996;36:715–25.
97. Xiong B, Li A, Lou Y, Chen S, Long B, Peng J, et al. Precise cerebral vascular atlas in stereotaxic coordinates of whole mouse brain. *Front Neuroanat.* 2017;11:128.
98. Calamante F, Thomas DL, Pell GS, Wiersma J, Turner R. Measuring cerebral blood flow using magnetic resonance imaging techniques. *J Cereb Blood Flow Metab.* 1999;19:701–35.
99. Pachitariu M, Sridhar S, Pennington J, Stringer C. Spike sorting with Kilosort4. *Nat Methods.* 2024;21:914–21.

ACKNOWLEDGEMENTS

We disclose support for the research of this work from the National Research Foundation of Korea (NRF; grant number RS2022NR067816 and grant number RS20040034357 to EL), the Ministry of Health & Welfare of Korea, Korea Health Industry Development Institute (KHIDI; grant number RS202400405260 and grant number RS202400438988 to EL), the Korea Institute of Science and Technology Information (grant number K24L2M1C4 to HK), and the Institute for Basic Science (IBS; grant number IBS-R015-D1 to SGK and grant number IBS-R002-D1 to EK).

AUTHOR CONTRIBUTIONS

J.K., S.L., Jisoo K., and G.L. conducted behavioral experiments and analyses. E.H., S.S., Y.G.K., J.K., Sooyeon L., S.K., and H.M. conducted electrophysiological experiments and analyses. J.K., S.L., H.J., S.J.K., H.Y.G., and H.K. conducted RNA-Seq analyses. H.J. conducted qPCR and immunoblot experiments. C.L. and S.C. conducted MRI experiments and analyses. H.Y.G., H.K., S.G.K., E.L., and E.K. designed the experiments and wrote the manuscript.

FUNDING

Open Access funding enabled and organized by KAIST.

COMPETING INTERESTS

The authors declare no competing interests.

ETHICS APPROVAL AND CONSENT TO PARTICIPATE

All animal experiments were performed in accordance with the relevant guidelines and regulations, including the Requirements of Animal Research at the Korea Advanced Institute of Science and Technology (KAIST). All experimental procedures

were reviewed and approved by the Committee on Animal Research at the Institute for Basic Science (IBS) (protocol number: IBS-2025-065). This study did not involve human participants, human tissue, or identifiable human data.

ADDITIONAL INFORMATION

Supplementary information The online version contains supplementary material available at <https://doi.org/10.1038/s41380-026-03646-9>.

Correspondence and requests for materials should be addressed to Eunee Lee or Eunjoon Kim.

Reprints and permission information is available at <http://www.nature.com/reprints>

Publisher's note Springer Nature remains neutral with regard to jurisdictional claims in published maps and institutional affiliations.



Open Access This article is licensed under a Creative Commons Attribution 4.0 International License, which permits use, sharing, adaptation, distribution and reproduction in any medium or format, as long as you give appropriate credit to the original author(s) and the source, provide a link to the Creative Commons licence, and indicate if changes were made. The images or other third party material in this article are included in the article's Creative Commons licence, unless indicated otherwise in a credit line to the material. If material is not included in the article's Creative Commons licence and your intended use is not permitted by statutory regulation or exceeds the permitted use, you will need to obtain permission directly from the copyright holder. To view a copy of this licence, visit <http://creativecommons.org/licenses/by/4.0/>.

© The Author(s) 2026